Sintering Ce-TZP/alumina composites using aluminum isopropoxide as a precursor

Sophie Cailliet, Marilyne Roumanie, Richard Laucournet, Guillaume Bernard-Granger

Sintering Ce-TZP/alumina composites using aluminum isopropoxide as a precursor

Sophie Cailliet[$], Marilyne Roumanie[$], Richard Laucournet[$] & Guillaume Bernard-Granger[*]

[$]Université Grenoble Alpes, CEA, LITEN, DTNM, 38000 Grenoble, France

[*]CEA, Nuclear Energy Division, Research Department on Mining and Fuel Recycling Processes, 30207 Bagnols-sur-Cèze, France

[*]*Corresponding author: guillaume.bernard-granger@cea.fr*

Abstract

A homogeneous 12Ce-TZP/30 vol% Al_2O_3 composite material has been manufactured by pressureless-sintering in air green compacts of a powder mixture incorporating aluminum isopropoxide as an organic precursor. Densification of the composite material occurs by grain boundary diffusion and is controlled by the diffusion of Ce cations.

Keywords

Zirconia; alumina; composites; sintering; microstructure

1. Introduction.

Since the discovery of transformation toughening [1-5] and toughening by ferroelastic domain switching [6], zirconia ceramic (ZrO_2) has been deeply investigated as a potential candidate for applications under severe mechanical conditions. For example, when the tetragonal phase is stabilized at room temperature by incorporating yttrium oxide as a dopant (formation of a solid solution), zirconia has been considered as the material of choice for hip and even knee prostheses in the nineties. Accordingly, around 600,000 zirconia femoral heads made of 3Y-TZP (3 mol% Y_2O_3, tetragonal zirconia polycristal) have been implanted in human body [7]. Unfortunately, at the beginning of the 2000's, an unexpected fracture episode of 3Y-TZP implanted femoral heads, belonging to a limited number of production batches from one of the leading manufacturer, was reported [7]. Its origin was related to the well-known low temperature degradation (LTD) mechanism encountered when such a material is subject to a humid environment [7-9]. LTD is a stress-amplified thermally activated process where tetragonal zirconia grains transform to monoclinic ones through a diffusionless-transformation (martensitic) [10-11].

Cerium cations may also be used as a stabilizing dopant for the zirconia tetragonal phase [12-13]. Cerium possesses the oxidation states III and IV. When a cerium oxide-stabilized zirconia polycristal is manufactured under air, cerium cations are in a tetravalent configuration, i.e. Ce^{4+}. Therefore, the substitution of Zr^{4+} cations by Ce^{4+} ones does not lead to the creation of oxygen vacancies but, nevertheless, allows a reduction in the density of oxygen anions around Zr^{4+} cations by a steric effect [14]. The lack of oxygen vacancy is responsible for the high LTD resistance of Ce-TZP polycrystalline materials in humid environments [8, 15] because the chemical species, in charge of the degradation, are not allowed to enter and diffuse into the zirconia lattice. It should be also emphasized that the sintering atmosphere, and thus the partial pressure of oxygen, can have an influence on the degree of oxidation of the cerium cations. This is even truer

when the raw samples initially contain a certain amount of organic additives (dispersant, binder, plasticizer ...) inherent to the manufacturing process used. Then, if Ce^{3+} cations are generated during the sintering step, they may also contribute to the stabilization of the tetragonal zirconia phase.

Accordingly, when the Ce content is tailored, Ce-TZP are thought to be interesting candidates for applications under humid environments and at moderate temperatures. Unfortunately and despite a much higher fracture toughness when compared to Y-TZP (values in the range 10-17 $MPa.m^{1/2}$ are achievable for Ce-TZP [16] against around 6-7 $MPa.m^{1/2}$ at maximum for Y-TZP [8]), Ce-TZP materials exhibit a much lower strength at room temperature (three-point bending strength around 500-800 MPa for Ce-TZP [16] against values as high as 1200-1500 MPa for Y-TZP [17]) mainly because of a much higher grain size (a too large tetragonal towards monoclinic phase transformation limits also strength) in the fully dense sintered polycrystalline material (above 1-2 µm for Ce-TZP [16] against 0.4-0.5 µm for Y-TZP [17]).

To be able to limit as much as possible grain growth in TZP materials and then to increase the strength, the adjunction of a minor second phase has been evaluated in the past [18-20]. The most remarkable result regarding the strength was obtained by Morita [18]. By combining high energy ball milling and spark-plasma sintering he reported three-point bending strength values as high as 2000 MPa for an almost fully-dense nanocrystalline composite made of 70 vol% of 3Y-TZP and 30 vol% of $MgAl_2O_4$ exhibiting a grain size for both phases around 100 nm.

In the approaches adopted by Morita, Nawa and Apel [18-20], the experiments were starting from mixtures of raw powders for elaborating the composites. Other investigators adopted another approach based on the preparation of high-solids-loading slurries incorporating organic precursors to be able to control the distribution and the size of the minor phase in different sort of sintered

nanostructured composites [21-26]. The main result concerning Ce-TZP-based nanocomposites has been reported by Reveron [23]. Fully-dense ceria-stabilized zirconia ceramics (84 vol% Ce-TZP) containing equiaxed alumina (8 vol% Al_2O_3) and elongated strontium hexa-aluminate (8 vol% $SrAl_{12}O_{19}$) second phases have been obtained by conventional pressureless-sintering [23]. The highest values in terms of biaxial bending strength and fracture toughness have been measured to be 1.1 GPa and above10 MPa.$m^{1/2}$, respectively, for a CeO_2 stabilizing content set to 10.5 mol% [23].

In the present paper we are presenting the preliminary results related to the development of a 12Ce-TZP/30 vol% Al_2O_3 composite using a chemical precursor to synthesize the alumina phase (a fully dense 12Ce-TZP polycrystalline material, having a grain size around 1 µm, has been shown to exhibit optimal bend strength around 800 MPa with a fracture toughness around 8 MPa.$m^{1/2}$ [16]. It was therefore considered that this composition was a good basis for the development of optimized zirconia-alumina composites). The conversion of the precursor to α-Al_2O_3 is briefly addressed as it is the core discussion of another upcoming paper. Different air sintering conditions are investigated, enabling the construction of the grain size/relative density trajectory for both phases. The microstructure and the chemical homogeneity of the sintered material is investigated. The activation energy for densification of the composite material is estimated and the mechanism controlling densification is discussed.

2. Experimental procedure.

2.1. Elaboration of the composite powder.

The commercially available CEZ-12 raw powder (Daiichi Kigenso Kagaku Kogyo CO., LTD, Osaka, Japan), stabilized in the tetragonal species by doping with 12 mol% of CeO_2, has been retained as the zirconia starting material. Because it has been proved to be a relevant choice by other investigators [27-28],

aluminum isopropoxide (flakes, $C_9H_{21}O_3Al$, purity ≥ 98%, Sigma Aldrich Chimie, Saint-Quentin-Fallavier, France) has been selected as the organic precursor for α-Al_2O_3. It should also be noted that an approach based on the use of a modified Pechini method was also evaluated at the same time to elaborate the composite powder [48]. However, the results proved to be less promising, particularly with regard to the uniformity of distribution of the zirconia and alumina phases after sintering. In addition to this, a first-level study of manufacturing costs showed that the modified Pechini approach was clearly less favorable [48]. Accordingly this way was quickly abandoned.

The first step of the 12Ce-TZP/30 vol% Al_2O_3 composite powder synthesis route is to disperse in acetone the adequate content of aluminum isopropoxide, using a planetary ball mill (Pulverisette 6, Fritsch GmbH, Idar-Oberstein, Germany), for 1 h with a fixed speed rate of 250 rpm. The jar and the grinding media are made of TZ3Y (polycrystalline tetragonal zirconia stabilized with 3 mol% of Y_2O_3). Grinding media are 20 mm diameter balls and the volume of the jar is 500 ml. The grinding media to powder ratio (in weight) is fixed to 2.3 (optimized using a design of experiment, DOE, approach). Then, the adequate content of CEZ-12 zirconia powder is incorporated into the jar and, in the same time, 3 wt% (in regard to the zirconia powder weight, the amount has been optimized using rheological tests) of Disperbyk 111 (dispersant, phosphoric acid polyester, Byk-Chemie GmbH, Wesel, Germany) is added. Finally, the jar containing all the ingredients and the grinding media is positioned again on the planetary ball mill during 1.5 h at 250 rpm (optimization of the dispersant content was carried out by means of sedimentation tests in test tubes, taking into account the presence of aluminum isopropoxide).

The powdered-mixture is recovered and dried under air, during 10 h, in a fume hood and a cake is finally obtained. A dry deagglomeration step is then performed by ball milling during 1 min at 250 rpm (same size/nature of jar and grinding media as before). A calcination step is then performed at 800 °C during

1 h in air (pure alumina crucibles are used, the heating rate is fixed to 300 °C/h, the temperature and duration have been tailored to ensure the removing of all organic compounds). Finally, the collected powder is gently crushed using a mortar and a pestle.

2.2. Sintering experiments.

Cylindrical samples with a diameter of 8 mm and a height of 5 mm have been prepared by uniaxial pressing of the gently-crushed calcined powder with a compaction pressure set to 150 MPa. By taking a theoretical density of 5.554 g/cm^3 for the target fully dense 12Ce-TZP/30 vol% Al_2O_3 composite formulation at room temperature (rule of mixture, a theoretical density of 6.230 g/cm^3 and 3.976 g/cm^3 is assumed for 12Ce-TZP and α-Al_2O_3, respectively), the relative green density is in all cases in the range 43-45% (calculated by assuming a complete conversion of aluminum isopropoxide to α alumina during the sintering step). Such values of the relative green density are a little bit low probably because the gently-crushing step of the calcined powder must be further optimized.

Dilatometer tests (vertical configuration, Setsys Evolution TMA, Setaram France, Caluire, France) in air have been conducted from room to soak temperature, using different heating rates (95, 258 and 443 °C/h), different soak temperatures (1300, 1400, 1500 and 1600 °C), different soak times (1, 2, 3 and 4 h) and a constant cooling rate (300 °C/h).

Assuming that the mass of the sample does not change significantly between the green and fired states (the weight loss is at maximum 2%), the following relationship is established [29-30]:

$$D_{(T)}(\%) = D_0(\%)\frac{1}{\xi^2\left[1+\frac{\Delta L_{(T)}}{L_0}\right]^3}e^{3\alpha(T-T_0)} \quad (2)$$

where $D_{(T)}$ is the instantaneous relative density of the sample at temperature T, D_0 is the relative green density at room temperature, ξ is representative of the shrinkage anisotropy of the sample during the test and is simply given by $\xi = (\phi_f/\phi_0)(L_0/L_f) = (\phi_{(T)}/\phi_0)(L_0/L_{(T)})$ with ϕ_f the final diameter, L_f the final height, ϕ_0 the initial diameter, L_0 the initial height, $\phi_{(T)}$ the instantaneous diameter, $L_{(T)}$ the instantaneous height, $\Delta L_{(T)} = L_{(T)} - L_0\ (< 0)$ the instantaneous sample height variation during the dilatometer test, α is the linear thermal expansion coefficient of the sample and T_0 is room temperature (20 °C). From a practical point of view, α is determined from the cooling steps of the dilatometer runs performed. An average value of 1.1459×10^{-5} /°C is retained.

After each dilatometer test, the density of the sintered sample was measured using the Archimedes method with deionized water (dry, immerged and humid masses are measured, three measurements were made for each sample). Then, as before, the relative density was obtained using a theoretical density of 5.544 g/cm^3 for the composite formulation investigated. For each sintered sample, a good agreement between the relative density measured using Archimedes method and the one obtained from the dilatometer curves was observed.

2.3. Crystallographic and microstructure investigations.

X-ray diffraction (XRD, Cu-K$_\alpha$ radiation with λ = 1.5406 Å, D5000, Bruker AXS SAS, Champs-sur-Marne, France) experiments have been completed on the aluminum isopropoxide starting flakes alone that have been calcined in air, during 1 h, at 800, 900, 1000, 1200 and 1300 °C (heating rate fixed to 300 °C/h, the flakes are positioned in an ultra-pure alumina crucible). XRD has been also used to characterize an almost fully-dense as-sintered composite sample (99.7%, sintered at 1600 °C during 1 h, heating rate fixed to 259 °C/h, cooling rate fixed to 300 °C/h, preparation of a polished surface).

Scanning electron microscopy observations (SEM, LEO 1530 Gemini®, Carl Zeiss S.A.S., Le Pecq, France) were completed on most of the sintered samples, on mirror polished surfaces annealed in air during 30 min at a temperature 100 °C below the sintering temperature to reveal grain boundaries. For each sintering condition, the grain size of zirconia and alumina phases has been determined using image analysis (Image J free software, developed by the National Institute of Health, United-States of America) on 150 grains of each species. The two-dimensional surface of each object appearing in the observation plan is measured and the diameter of a corresponding disc having the same surface value is calculated (a tridimensional correction factor of 1.2 is used [31]). Then, knowing for each sample the sintered relative density and the average grain size for alumina and zirconia grains, the two-dimension sintering trajectory (evolution of the grain size versus the relative density) for both phases is constructed. In addition to this, using the same methodology, the average residual pore diameter is determined for each sintered sample and the evolution of the residual pore size as a function of the relative density of the sintered samples is analyzed (we are aware that the pore size measured will be possibly affected by the annealing step needed to reveal grain boundaries, as it will be also possibly the case for the grain size itself).

In parallel to SEM observations, energy dispersive X-ray spectroscopy (EDS, Esprit, Bruker Nano GmbH, Berlin, Germany) analyses in map mode have been completed on a few as-sintered samples. This mode has been especially retained to investigate the alumina phase distribution in an almost fully dense sample (99.7%, sintered at 1600 °C during 1 h, heating rate fixed to 259 °C/h, cooling rate fixed to 300 °C/h). EDS maps are acquired (acquisition time fixed to 10 min, acceleration voltage fixed to 15 kV, working distance fixed to 10 mm and condenser diaphragm set to 60 µm) at magnifications of 500, 1000, 2000, 5000 and 10000. Then, for each map, a global quantification is performed regarding Zr, Al, Ce and O elements (PhiRhoZ method with internal standards of the Esprit

software and assuming a Gaussian deconvolution of each peak). For each magnification the (weight%/weight%) Al/Zr, Al/O, Zr/O and Ce/Zr ratio are calculated.

Transmission electron microscopy (TEM) and scanning transmission electron microscopy (STEM, a high angle annular dark field – HAADF – detector is used) observations (Tecnai Osiris, FEI, Eindhoven, Netherlands, acceleration voltage of 200 kV, point to point resolution of 2.5 Å) coupled to EDS analyses (Esprit, Bruker Nano GmbH, Berlin, Ge) using four quadrant SDD detectors (ChemiStem technology, FEI, Eindhoven, Netherlands) have been performed on both kind of samples. Firstly the composite powder before calcination and powders after calcination at 800, 900, 1000, 1200 and 1300 °C have been investigated by dispersing the samples in pure ethanol and deposing them on an amorphous carbon grid. Secondly, the deep microstructure of an almost fully dense sintered sample (99.7%, sintered at 1600 °C during 1 h, heating rate fixed to 259 °C/h, cooling rate fixed to 300 °C/h) is also observed. For that a thin foil was prepared using focused ion beam (Strata DB 235, FEI, Eindhoven, Netherlands). For both kind of samples complementary observations have also been performed using the high-resolution transmission electron microscopy (HRTEM) mode. Additionally, whatever the kind of sample, quantitative EDS analyses are also performed in point mode when needed (Cliff-Lorimer method with theoretical k-factors calculated under Esprit software for an acceleration voltage of 200 kV). It should be noted that none of the samples observed were metallized beforehand.

3. Results and discussion.

Fig. 1a shows the microstructure in TEM bright field mode of the as-synthesized composite powder before the calcination step at 800 °C. Individual crystalline grains having a polygonal shape and an averaged size in the range 40-300 nm are

observed. Some exhibit twins (blue arrow), even if this trend remains occasional. These grains are surrounded by a fluffy second phase (yellow arrows).

At higher magnifications (Fig. 1b) the fluffy phase appears devoid of any significant ordering, as it is confirmed using the HRTEM mode (Fig. 1c). The fast Fourier transformation (FFT, Fig. 1d) of a given region of interest of the fluffy phase (yellow square on Fig. 1c) exhibits mainly amorphous rings with also few tiny spots proving that some crystalline entities are also possibly present.

Fig. 2 shows EDS maps acquired in STEM mode on the same area as the one observed in TEM bright field mode and reported on Fig. 1. The polygonal individual grains contain Zr and O and have the ZrO_2 composition. Most of these grains contain also the stabilizing dopant Ce and quantitative EDS analyses show that the content is around 3.9 at%, not too far from the target one (4 at% for a zirconia composition incorporating 12 mol% of CeO_2 as a dopant).

Nevertheless, it is interesting to point out that the twinned grain reported on Fig. 1 (white arrow on Fig. 2) is clearly depleted in Ce in comparison to the other surrounding ones. Even if it has not been scrupulously verified, such grains detected occasionally are probably made of non-stabilized monoclinic zirconia. It also appears that the fluffy phase is made of Al and O and a quantitative EDS analysis confirms the composition Al_2O_3. It is also important to underline that all the areas investigated on the carbon supporting grid show a homogeneous mixture of zirconia and alumina based compounds without any segregation of alumina or zirconia heap.

Fig. 3 shows XRD patterns acquired on the aluminum isopropoxide precursor alone after air calcination at temperatures ranging from 800 to 1200 °C. Even if it is the core of another paper, it must be emphasized that the conversion of aluminum isopropoxide to crystalline α-Al_2O_3 seems almost completed at a

temperature as high as 1200° C. For temperatures below 1200 °C, the precursor remains mostly amorphous even if some diffraction peaks belonging to transition alumina species are identified. However, it is useful to remember that the XRD detection limit of an oxide phase is around 5-10%. As a result, XRD does not make it possible to optimally detect any traces of residual transition alumina.

Indeed, as it will be also reported in a separate paper, HRTEM observations on the composite powder calcined at different temperatures show that a full conversion of the precursor into the α-Al_2O_3 phase occurs at 1300 °C only, as reported on Fig. 4 (the FFT of the region of interest in zirconia and alumina crystalline areas are compatible to the tetragonal and α phase, respectively).

Below this temperature nanocrystalline domains belonging to different transition alumina species are detected for calcination temperatures fixed to 900, 1000 and 1200 °C. When the calcination temperature is set to 800 °C, the precursor remains amorphous. As a result, it appears that the conversion of aluminum isopropoxide to α alumina occurs at a higher temperature (around 100 ° C above) in the case of the composite powder compared to isopropoxide alone.

Fig. 5 shows the variation of the densification rate in air, in the range 500-1600 °C (below 500 °C, the curves remains flat), for the composite powder calcined at 800 °C, the zirconia powder alone and aluminum isopropoxide precursor alone.

The maximum densification rate is measured at 1140 and 1280 °C for aluminum isopropoxide and CEZ-12 zirconia, respectively. Densification rate vanishes around 1200 °C for aluminum isopropoxide and around 1500 °C for zirconia. The densification rate for the composite powder exhibits two distinct peaks: one at 1240 °C and another one at 1415 °C. Densification rate vanishes around 1600 °C (slightly above in fact) for the composite powder. It has also to be outlined

that 1300 °C (dark-dotted line on Fig. 5) is the key temperature where the second densification rate peak begins to form. Accordingly, by taking also into account the results reported above from XRD analyses and HRTEM observations regarding the calcination of aluminum isopropoxide and the composite powder, the following scenario is advanced. The composite powder begins to sinter around 950 °C. In a first step, between 950 and 1300 °C, aluminum isopropoxide transforms to α-Al_2O_3 (transiting through the different transition alumina phases) which generates the first densification rate peak due to particles rearrangement and probably local sintering. Above 1300 °C, the alumina-zirconia composite densifies. The maximum densification rate temperature and the temperature where densification rate vanishes are shifted towards higher temperatures (100 °C above), in comparison to pure zirconia, because α alumina second phase acts as an obstacle regarding the diffusion mechanisms involved. Indeed, the alumina conversion step towards the α phase is known to generate a network of wormy/vermicular grains [45-47] that could limit further rearrangement possibilities and have an impact on densification.

Fig. 6a shows the two-dimension sintering trajectories for the zirconia and alumina phases (for each sample the sintering conditions are described by "Heating rate value in °C/h – Soak temperature in °C – Soak time in h" triplets, in all cases the cooling rate was fixed to 300 °C/h). Whatever the sintering parameters and the phase considered, all the points align on a single trajectory, as it was already reported for monolithic oxide-based polycrystalline ceramics [29-30, 32] and alumina-zirconia (Y as the tetragonal-phase stabilizer or no stabilizer used) composites [33] pressureless-sintered in air. In all cases, the trajectory for alumina grains remain below the one for zirconia grains. It is only for sintering temperatures above 1500 °C and for sintered relative density higher than 99 % that the grain size of alumina and zirconia grains increases sharply. Accordingly, it is possible to obtain a 98% dense sample with zirconia and alumina grains having an average diameter around 1.1 and 0.8 µm, respectively.

Fig. 6b shows the variation of the average diameter of residual pores in function of the post-sintering relative density of the different samples investigated. For relative densities in the range 70-95%, the residual pore diameter decreases slightly when the relative density increases. For post-sintering relative densities higher than 95%, the residual pore diameters increases significantly with the increase in density. Such a value is in agreement with the transition from an opened (intermediate stage) to a closed (final stage) porosity during sintering polycristalline materials [34]. Finally, as depicted on Fig. 6c, it appears that the average grain size of alumina grains is a linear function of the average grains size of zirconia ones.

The microstructure development during sintering of the composite material is resumed on Fig. 7, for a magnification set to the same value (X5000) for the different samples observed (SEM observations in secondary electron mode, the alumina phase is the darker one). Fig. 7a shows the typical microstructure for a post-sintered sample having a relative density around 73% (heating rate fixed to 300 °C/h, 2 h soak at 1300 °C, cooling rate fixed to 300 °C/h, see sintering trajectories on Fig. 6a). Densification seems inhomogeneous with islands not as dense as the surrounding material that contains also a high amount of residual pores. Zirconia and alumina grains are very small and difficult to identify for this magnification.

The microstructure for a sample sintered to a relative density around 88% (heating rate fixed to 600 °C/h, 1 h soak at 1400 °C during 1 h, cooling rate fixed to 300 °C/h, see sintering trajectories on Fig. 6a) is shown on Fig. 7b. Some porous islands are still there. The densification in the material surrounding the islands is significantly enhanced in comparison to the sample sintered to 73% relative density. Alumina grains are now clearly identified and appear homogeneously dispersed throughout the sample. Fig. 7c shows the typical microstructure for a post-sintered sample having a relative density around 91% (heating rate fixed to 300 °C/h, 3 h soak at 1400 °C, cooling rate fixed to 300

°C/h, see sintering trajectories on Fig. 6a). Only few porous islands are now detected, some of them having however a large size (some tens micrometer in diameter). The material surrounding the islands is almost fully dense with only few tiny pores remaining. The alumina phase is globally homogeneously dispersed even if some few micrometer-sized heaps are observed. Finally, the microstructure for a sample sintered to a relative density around 99.4% (heating rate fixed to 300 °C/h, 4 h soak at 1500 °C, cooling rate fixed to 300 °C/h, see sintering trajectories on Fig. 6a) is shown on Fig. 7d. All porous heaps have now disappeared. Some residual and isolated pores are distributed throughout the sample. Their number appears higher than the one observed in the material surrounding the porous heaps for the sample sintered to 91% relative density confirming porosity redistribution when entering in the final sintering stage. Alumina grains are always homogeneously dispersed even if some clusters are sometimes always observed. Concerning the presence of porous islands in the microstructure they possibly result from aggregation during the powder manufacturing process. When present in the raw powder used to press green pellets, they probably have an internal structure (porosity amount, interlocking structure, for example) and a mechanical strength which promote the presence of relics in the shaped samples that are more difficult to resorb during sintering in comparison to the surrounding material. Preliminary SEM/EDS investigations show that some of the porous islands are also enriched in Al, attesting probably some segregation and agglomeration problems. However, what is surprising is that these kind of clusters are very rarely detected in a material having a post-sintering density greater than 99% (it has been scrupulously verified on different samples at different magnifications, see the one highlighted by the yellow arrow on Fig. 7d as an example). Complementary investigations are running to clarify this point.

Fig. 8 shows the XRD pattern acquired on an almost fully dense composite sample after sintering (99.7 %, heating rate fixed to 300 °C/h, 1 h soak at 1600 °C, cooling rate fixed to 300 °C/h, see sintering trajectories on Fig. 6a). Only two

phases are detected: $Ce_{0.12}Zr_{0.88}O_2$ tetragonal zirconia (t, 04-006-7961 JCPDS file) and α-alumina (α, 04-004-2852 JCPDS file).

The typical microstructure of an almost fully dense composite sample (99.7 %, heating rate fixed to 300 °C/h, 1 h soak at 1600 °C, cooling rate fixed to 300 °C/h, see sintering trajectories on Fig. 6a) observed by TEM in bright field mode is reported on Fig. 9. Most of alumina grains (the white ones) appear attached to the grain boundaries of the zirconia grains, promoting most probably a pinning effect during sintering. The shape of alumina grains is also more rounded/lenticular. Even if the zirconia grains exhibit a more polygonal morphology, the presence of alumina grains may favor an unbalanced configuration in certain areas (pink arrows on Fig. 9). Few very small alumina grains appear also entrapped in zirconia ones (yellow arrow on Fig. 9).

For the same investigated area, Fig. 10 shows a STEM/HAADF picture with the corresponding EDS maps for the Zr, Ce, O and Al chemical elements. Ce-enriched areas are observed at the zirconia-alumina triple points (pink-doted ellipses on Fig. 10). Several quantitative EDS analyses in point-mode in zirconia grains give an average chemical composition of 66.5 at% O, 29.1 at% Zr, 3.3 at% Ce, 0.8 at % Al and 0.3 at% Hf (hafnium is a well-known impurity for zirconia). In comparison to what was measured in the zirconia crystallites constituting the composite starting powder (3.9 at%, see before), there is a depletion of 0.6 at% in Ce in the individual zirconia grains constituting the sintered polycrystalline composite sample. Accordingly, some Ce is leaving zirconia grains during sintering to segregate at triple points. This is probably related to the oxygen partial pressure of the sintering atmosphere close to the sample, promoting a valence change from Ce^{4+} to Ce^{3+} (for a coordination number fixed to 8, the ionic radius of a Ce^{3+} cation is larger than the one of a Ce^{4+} cation, 114 ppm against 97 ppm, respectively). Then the largest Ce^{3+} cations are expulsed from the zirconia grains. It is also interesting to point out that around 0.8 at% of Al is present in the zirconia grains, attesting that they are pumping

some aluminum from the alumina ones (the content of Al was null in the zirconia elemental crystallites constituting the composite powder). Guo reported a solubility limit around 1 wt% for alumina in 8-mol%-Y_2O_3-stabilized ZrO_2 at 1500 °C [44]. This gives an aluminum concentration equal to 0.8 at%, in perfect agreement with what is measured in the zirconia grains of the sintered composite investigated. In the same time, quantitative EDS analyses, also performed in point-mode, have shown that alumina grains are devoid of any other chemical element than Al and O.

Figs. 11a and 11b show the typical microstructures of a 100% 12Ce-TZP sample and a 12Ce-TZP/30 vol% Al_2O_3 composite sample green-shaped by uniaxial pressing and sintered in exactly the same conditions (heating rate fixed to 300 °C/h, 1 h soak at 1600 °C, cooling rate fixed to 300 °C/h), respectively. The post-sintering relative densities are measured to be 99.7 and 100% for the composite and pure zirconia materials, respectively. It clearly appears that the grain size of zirconia grains is significantly reduced in the composite sample, as confirmed by the comparison of the zirconia grain size distribution for both samples and shown on. Fig. 11c. Alumina grains in the composite sample exert a pinning pressure on zirconia grain boundaries that reduces their mobility and minimizes grain growth as described by Smith in the late forties for the analysis of grain growth in particles-containing materials [35]. Fig. 11d shows the evolution of the elements ratio, determined by quantitative EDS analyses, for a 99.7% dense composite sample (heating rate fixed to 300 °C/h, 1 h soak at 1600 °C, cooling rate fixed to 300 °C/h) observed under SEM at different magnifications. It appears that each elements ratio is independent on the magnification used for the quantification, which attests to the good chemical homogeneity of the analyzed sample at different scales. Whatever the magnification, the global composition 12Ce-TZP/34 vol% Al_2O_3 is calculated for the composite, which is not too far from the 12Ce-TZP/30 vol% Al_2O_3 target one if we assume the validity of the Delesse's law [49] where the surface fraction of a given phase equals its volume fraction when observing a flat polished surface.

Let us now discuss about the densification mechanism possibly involved during pressureless-air-sintering in the 12Ce-TZP/30 vol% Al_2O_3 composite formulation investigated. Fig. 12a shows the densification curves in air, calculated using equation (2), for the composite powder (calcined à 800 °C during 1 h, in air, before shaping the green compacts) and for different heating rate values.

The maximum relative density value is limited to 90% because above it is not possible to do a clear distinction between densification curves obtained for heating rates fixed to 258 and 443 °C/h. Whatever the heating rate, the samples start to densify around 900 °C. For temperatures higher than 1150 °C, the lower is the heating rate, the higher is the relative density for a given temperature. This is a well-known trend, already observed for a lot of ceramic oxide-based formulations [29-30, 32, 36-37]. By using a lower heating rate, a compacted powder sample is thermally exposed for a longer time and shrinks more before reaching a target temperature [36]. Whatever the heating rate used, it is also important to note that the densification curve has a wavy shape.

From each densification curve, the instantaneous absolute densification rate is then calculated, point by point, using the following expression [29-30]:

$$\frac{1}{D_{(T)}}\frac{dD_{(T)}}{dt} = \frac{1}{D_{(T)}}\frac{D_{T+\delta T}^{t+\delta t} - D_{T-\delta T}^{t-\delta t}}{2\delta t} \quad (3)$$

where δt is the time difference between two points acquisition when the difference of temperature is δT. The variation of the absolute densification rate in function of temperature for the different heating rate values retained is shown on Fig. 12b. Whatever the temperature, the higher the heating rate, the higher the instantaneous densification rate. Whatever the heating rate, two peaks are observed (wavy-shape densification curves). The higher the heating rate, the more the maxima of these two peaks are shifted to high temperatures. As justified

before using XRD experiments and TEM observations, the first peak is related to the conversion of aluminum isopropoxide to α alumina. The second peak is then devoted to the densification of the resulting zirconia/alumina material. At this stage, it is therefore important to note that the use of a high heating rate will shift to the high temperatures the precursor conversion and sintering steps of the powder medium. Fig. 12c is even more interesting. It shows the evolution of the instantaneous thermal densification rate, $\frac{1}{D_{(T)}}\frac{dD_{(T)}}{dT}$,in function of the relative density for the different heating rate values retained for our investigations. All the points align now on an almost single curve. The first rate peak, related to the conversion of aluminum isopropoxide to α-Al_2O_3, belongs to the 43-65% relative density range. The second one, in connection with the densification of the zirconia-alumina composite, is in the relative density range 65-90%. To be able to calculate activation energy values for the conversion and densification steps, it has been decided to focus our attention on the 47-60% (black-doted lines on Fig. 12c) and 66-85% (grey-dotted lines on Fig. 12c) relative density domains, respectively.

In most cases, the equation for the densification rate can be separated into temperature-dependent, grain size-dependent and density-dependent quantities as follows [29-30, 33]:

$$\frac{dD_{(T)}}{dt} = A\frac{F\left[D_{(T)}\right]}{G^n}\frac{e^{-\frac{Q_d}{RT}}}{T} \quad (4)$$

where:

- A is a constant,
- $F\left[D_{(T)}\right]]$ is a function only of density,
- Q_d is the apparent activation energy for the mechanism controlling densification,

- R is the perfect gas constant,
- T is the absolute temperature,
- G is the grain size,
- n is the grain size exponent and its value depends on whatever the densification rate is controlled by lattice diffusion ($n = 3$) or by grain-boundary diffusion ($n = 4$).

The instantaneous densification rate may be also written as:

$$\frac{dD_{(T)}}{dt} = \frac{dD_{(T)}}{dT}\frac{dT}{dt} \quad (5)$$

where $\frac{dT}{dt}$, the heating rate, is held constant during the dilatometer tests performed.

By combining relations (4) and (5) we obtain:

$$Ln\left[T\frac{dD_{(T)}}{dT}\frac{dT}{dt}\right] = -\frac{Q_d}{RT} + Ln\{F[D_{(T)}]\} + Ln(A) - nLn(G) \quad (6)$$

A plot of the left-hand side versus $\frac{1}{T}$ would give a value for Q_d provided that the data points are taken at a constant value of $D_{(T)}$ and G. If the grain size is not changing significantly during the experiments, points for a constant value of $D_{(T)}$ are obtained by changing the heating rate. The measurements lead to values of Q_d at different values of $D_{(T)}$. This formalism is known as the CRH one and has been applied since a long time for the investigation of sintering [33, 36-37, 38]. From a practical point of view, the T and $\frac{dD_{(T)}}{dT}$ values at the same relative density are determined from vertical dilatometer curves obtained at different fixed heating rates. Then their values are plotted as an Arrhenius-type plot of $T\frac{dD_{(T)}}{dT}\frac{dT}{dt}$ against $\frac{1}{T}$. The apparent activation energy, Q_d, of the mechanism controlling

densification is then determined from the slope of the straight line in the Arrhenius-type plot.

Assuming that the average grain size (alumina and zirconia) of the composite material investigated is constant during our sintering experiments for relative density values below 85% (it is not scrupulously true, because the crystallite size in the starting zirconia powder is at maximum around 300 nm, the sintering trajectories on Fig. 6a for alumina and zirconia grains are not scrupulously flat for relative densities below 90%), Fig. 13a shows the plots of $Ln\left[T\frac{dD_{(T)}}{dT}\frac{dT}{dt}\right]$ in function of $\frac{1}{T}$ (CRH analysis) for different relative densities belonging to the global range 53-80 %. For densities ranging from 53 to 60%, the straight lines obtained are not parallel. Conversely, when the relative density is between 60 and 80%, the lines are almost parallel.

On Fig. 13b is shown the variation of the activation energy value for densification in function of the relative density and calculated from the slopes obtained on Fig. 13a. When the relative density is in the range 53-60%, which corresponds to the interval where aluminum isopropoxide converts to α alumina, the activation energy for densification linearly increases. For relative densities between 60 and 80%, the activation energy for densification of the zirconia-alumina composite has an almost constant value around 450 kJ/mol. In a recent paper, new relationships between the grain size and the relative density have been established during solid-state sintering of ceramic powders [39]. By taking into account a mixing rule, based on the volume fraction of the zirconia and alumina phases present in the composite formulation, a global average grain size (*G*) for each sintered sample used to construct the sintering trajectories shown on Fig.6a has been calculated. Then the (grain size, relative density) pairs have been interpolated with the different expressions from [39]. As shown on Fig. 13c, the best coefficient of determination (0.9875) is obtained for a linear interpolation of $1/G^2$ in function of the post-sintering relative density, which means that

densification of the composite investigated occurs by grain boundary diffusion and grain growth is controlled by the grain boundaries [39]. Fig. 13d shows the volume and grain boundary diffusion coefficients for Zr, O and Ce in different kinds of zirconia polycrystals (tetragonal and cubic phase, Y and Ca as stabilizers), in the temperature range 1200-1600 °C, taken from the literature [40-43]. Densification is controlled by the slower species travelling by the fastest path. Whatever the chemical element, grain boundary diffusion coefficients are much higher than volume ones. It is for Ce that the grain boundary diffusion coefficient is the slowest one on all the temperature range of interest. The activation energy for the grain boundary diffusion of Ce in zirconia is around 500 kJ/mol, which is not too far from 450 kJ/mol, the activation energy determined for the densification step of the zirconia-alumina composite material investigated. Consequently, we may advance that densification of the composite material is carried out by diffusion at the grain boundaries and is controlled by the diffusion of the Ce cations. The fact that cerium cations segregate at triple points of the sintered microstructure attests to a primordial contribution of their displacement with respect to the mechanism controlling the densification of the composite.

4. Conclusion.

Pressureless-sintering of a 12Ce-TZP/30 vol% Al_2O_3 composite powder, using aluminum isopropoxide as an organic precursor to synthesize the alumina phase, has been investigated in air, up to 1600 °C.

Densification takes place in two phases: i) in the 43-65% relative density range aluminum isopropoxide transforms to α alumina, ii) above 65% relative density densification of the zirconia-alumina composite takes place. It was also shown that densification occurs by grain boundary diffusion and is controlled by the diffusion of the Ce cations.

It was possible to manufacture a 98% dense material with a zirconia grain size of 1.1 µm, an alumina grain size of 0.8 µm and with a homogeneous distribution of the alumina phase. The next step will be to measure its mechanical properties (flexural strength, fracture toughness and hardness) at room temperature. The possibility of making such a material by 3D printing (stereolithography) will be also evaluated.

References

[1] R.C. Garvie, R.H. Hannink, R.T. Pascoe. Ceramic Steel ? *Nature* 258 (1975) 703-704

[2] A.H. Heuer, N. Claussen, W.M. Kriven, M. Rühle. Stability of tetragonal ZrO_2 particles in ceramic matrices. *J Am Ceram Soc*. 65 (1982) 642-650

[3] R.M. McMeeking, A.G. Evans. Mechanics of transformation toughening in brittle materials. *J Am Ceram Soc*. 65 (1982) 242-246

[4] F.F. Lange. Transformation toughening. Part 1. Size effects associated with the thermodynamics of constrained transformations. *J Mater Sci*. 17 (1982) 225-234

[5] B. Budiansky, J. Hutchinson, J. Lambroupolos. Continum theory of dilatant transformation toughening in ceramics. *Int J Solids Struct*. 19 (1983) 337-355

[6] A.V. Virkar, R.L.K. Matsumoto. Ferroelastic domain switching as a toughening mechanism in tetragonal zirconia. *J Am Ceram Soc*. 69 (1968) C224-C226

[7] J. Chevalier, L. Gremillard, A.V. Virkar, D.R. Clarke. The tetragonal-monoclinic transformation in zirconia: lessons learned and future trends. *J Am Ceram Soc.* 92 (2009) 1901-1920

[8] J. Chevalier, B. Cales, J.-M. Drouin. Low-temperature aging of Y-TZP ceramics. *J Am Ceram Soc*. 82 (1999) 2150-2154

[9] J. Chevalier. What future for zirconia as a biomaterial ? *Biomaterials*. 27 (2006) 535-543

[10] S. Deville, G. Guénin, J. Chevalier. Martensitic transformation in zirconia. Part I. Nanometer scale prediction and measurement of transformation induced relief. *Acta Mater*. 52 (2004) 5697-5707

[11] S. Deville, G. Guénin, J. Chevalier. Martensitic transformation in zirconia. Part II. Martensite growth. *Acta Mater*. 52 (2004) 5709-5721

[12] T.W. Coyle, W.S. Coblenz, B.A. Bender. Toughness, strength and microstructures of sintered CeO_2 and doped ZrO_2 alloys. *Am Ceram Soc Bull*. 62 (1983) 966-967

[13] F.F. Lange. Transformation toughening. Part 5: Effect of temperature and alloy on fracture toughness. *J Mater Sci*. 17 (1982) 255-262

[14] P. Li, I.W. Chen, J.E. Penner-Hahn. Effect of dopants on zirconia stabilization – An X-ray absorption study: II, Tetravalant dopants. *J Am Ceram Soc*. 77 (1994) 1281-1288

[15] N. Courtois. Nouveaux matériaux céramiques à base de zircone pour application dentaire. Ph.D. Thesis, INSA-Lyon, France, (2011)

[16] K. Tsukuma, M. Shimada. Strength, fracture toughness and Vickers hardness of CeO_2-stabilised tetragonal ZrO_2 polycrystals (Ce-TZP). *J Mat Sci*. 20 (1985) 1178-1184

[17] K. Tsukuma K, Y. Kubota, T. Tsukidate. Thermal and mechanical properties of Y_2O_3-stabilized tetragonal zirconia polycrystals. *Advances in Ceramics, Vol.*

12, Science and Technology of Zirconia II. Edited by N. Claussen, M. Rühle, and A. H. Heuer, American Ceramic Society, Columbus, OH, p382-390, (1984)

[18] K. Morita, K. Hiraga, B.-N. Kim, H. Yoshida, Y. Sakka. Synthesis of dense nanocrystalline ZrO_2–$MgAl_2O_4$ spinel composite. *Scripta Mater*. 53 (2005) 1007-1012

[19] M. Nawa, S. Nakamoto, T. Sekinob, K. Niihara. Tough and strong Ce-TZP/alumina nanocomposites doped with titania. *Ceram Int*. 24 (1998) 497-506

[20] E. Apel, C. Ritzberger, N. Courtois, H. Reveron, J. Chevalier, M. Schweiger, F. Rothbrust, V.M. Rheinberger, W. Höland. Introduction to a tough, strong and stable Ce-TZP/$MgAl_2O_4$ composite for biomedical applications. *J Eur Ceram Soc*. 32 (2012) 2697-2703

[21] P. Palmero, L. Montanaro, H. Reveron, J. Chevalier. *Materials* 7 (2014) 5012-5037

[22] P. Palmero a, M. Fornabaio, L. Montanaro, H. Reveron, C. Esnouf, J. Chevalier. Towards long lasting zirconia-based composites for dental implants. Part I: Innovative synthesis, microstructural characterization and in vitro stability. *Biomaterials* 50 (2015) 38-46

[23] H. Reveron, M. Fornabaio, P. Palmero, T. Fürderer, E. Adolfsson, V. Lughi, A. Bonifacio, V. Sergo, L. Montanaro, J. Chevalier. Towards long lasting zirconia-based composites for dental implants: Transformation induced plasticity and its consequence on ceramic reliability. *Acta Biomater.* 48 (2017) 423–432

[24] P. Palmero, V. Naglieri, G. Spina, M. Lombardi. Microstructural design and elaboration of multiphase ultra-fine ceramics. *Ceram Inter.* 37 (2011) 139–144

[25] P. Palmero, A. Sola, V. Naglieri, D. Bellucci, M. Lombardi, V. Cannillo. Elaboration and mechanical characterization of multi-phase alumina-based ultra-fine composites. *J Mater Sci.* 47 (2012) 1077–1084

[26] M. Schehl, L.A. Diaz, R. Torrecillas. Alumina nanocomposites from powder–alkoxide mixtures. *Acta Mater.* 50 (2002) 1125–1139

[27] T.Q. Nguyen, K.Y. Park, K.Y. Jung, S.B. Cho. Vapor-phase synthesis of a solid precursor for α-alumina through a catalytic decomposition of aluminum triisopropoxide. *Mater Res Bull*. 46 (2011) 2199-2203

[28] L. Xu, H. Song, L. Chou. Facile synthesis of nano-crystalline alpha-alumina at low temperature via an absolute ethanol sol–gel strategy. *Mater Chem Phys*. 132 (2012) 1071-1076

[29] G. Bernard-Granger, C. Guizard. Apparent activation energy for the densification of a commercially available granulated zirconia powder. *J Am Ceram Soc*. 90 (2007) 1246-1250

[30] N. Benameur, G. Bernard-Granger, A. Addad, S. Raffy, C. Guizard. Sintering analysis of a fine-grained alumina–magnesia spinel powder. *J Am Ceram Soc*. 94 (2011) 1388-1396

[31] G. Bernard-Granger, C. Guizard, A. Addad. Influence of co-doping on the sintering path and on the optical properties of a submicronic alumina material. *J Am Ceram Soc*. 91 (2008) 1703-1706

[32] G. Bernard-Granger, C. Guizard, A. Addad. Sintering of an ultra pure α-alumina powder. I. Densification, grain growth and sintering path. *J Mater Sci*. 42 (2007) 6316-6324

[33] J. Wang, R. Raj. Activation energy for the sintering of two-phase alumina/zirconia ceramics. *J Am Ceram Soc*. 74 (1991) 1959-1963

[34] R.M. German. Sintering – From Empirical observations to scientific principles. Elsevier, Waltham, MA, USA, (2014)

[35] C.S. Smith. Grains, phases, and interphases – An interpretation of microstructure. *Trans Metal Soc AIME*. 175 (1948) 15-51

[36] E. Sato, C. P. Carry. Yttria doping and sintering of submicrometer-grained α-alumina. *J Am Ceram Soc*. 79 (1996) 2156-2160

[37] J. Wang, R. Raj. Estimate of the activation energies for boundary diffusion from rate-controlled sintering of pure alumina and alumina doped with zirconia and titania. *J Am Ceram Soc*. 73 (1990) 1172-1175

[38] W. S. Young, I. B. Cutler. Initial sintering with constant rates of heating. *J Am Ceram Soc.* 53 (1970) 659-663

[39] G. Bernard-Granger, C. Guizard. New relationships between relative density and grain size during solid-state sintering of ceramic powders. *Acta Mater*. 56 (2008) 6273-6282

[40] S. Swaroop, M. Kilo, C. Argirusis, G. Borchardt, A.H. Chokshi. Lattice and grain boundary diffusion of cations in 3YTZ analyzed using SIMS. *Acta Mater*. 53 (2005) 4975-4985

[41] L.A. Simpson, R.E. Carter. Oxygen exchange and diffusion in calcia-stabilized zirconia. *J Am Ceram Soc*. 49 (1966) 139-144

[42] G. Knöner, K. Reimann, R. Röwer, U. Södervall, H.-E. Schaefer. Enhanced oxygen diffusivity in interfaces of nanocrystalline $ZrO_2.Y_2O_3$. *PNAS*. 100 (2003) 3870-3873

[43] V. Menvie Bekale, A.M. Huntz, C. Legros, G. Sattonnay, F. Jomard. Impurity diffusion of cerium and gadolinium in single and polycrystalline yttria-stabilized zirconia. *Phil Mag*. 88 (2007) 1-19

[44] X. Guo. Roles of alumina in zirconia for functional applications. *J Am Ceram Soc.* 86 (2003) 1867-1873

[45] F. W. Dynys, J. W. Halloran. Alpha alumina formation in alum-derived gamma alumina. *J Am Ceram Soc.* 65 (1982) 442-448

[46] C. Legros, C. Carry, P. Bowen, H. Hofmann. Sintering of a transition alumina: Effects of phase transformation, powder characteristics and thermal cycle. *J Eur Ceram Soc.* 19 (1999) 1967-1978

[47] P. Palmero, M. Lombardi, L. Montanaro, M. Azar, J. Chevalier, V. Garnier, Gilbert Fantozzi. Effect of heating rate on phase and microstructural evolution during pressureless sintering of a nanostructured transition alumina. *Int J Appl Ceram Technol.* 6 (2009) 420–430

[48] S. Cailliet: Développement de composants céramiques en zircone stabilisée par stéréolithographie pour applications dentaires. Ph.D. Thesis, Université Grenoble Alpes, France, (2018)

[49] M. A. Delesse. Procédé mécanique pour déterminer la composition des roches. *CR Acad Sci.* 25 (1847) 544-545.

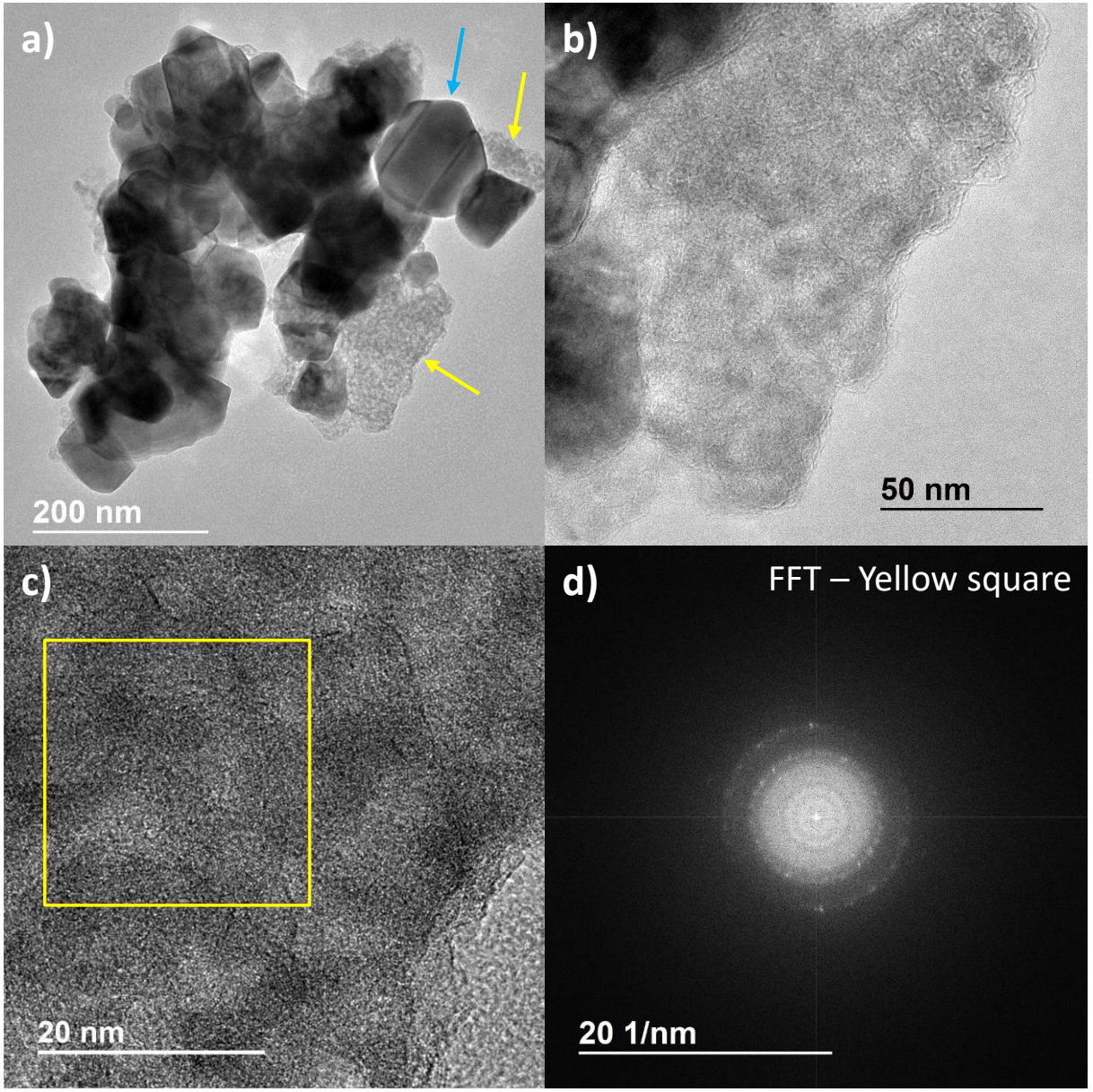

Fig. 1

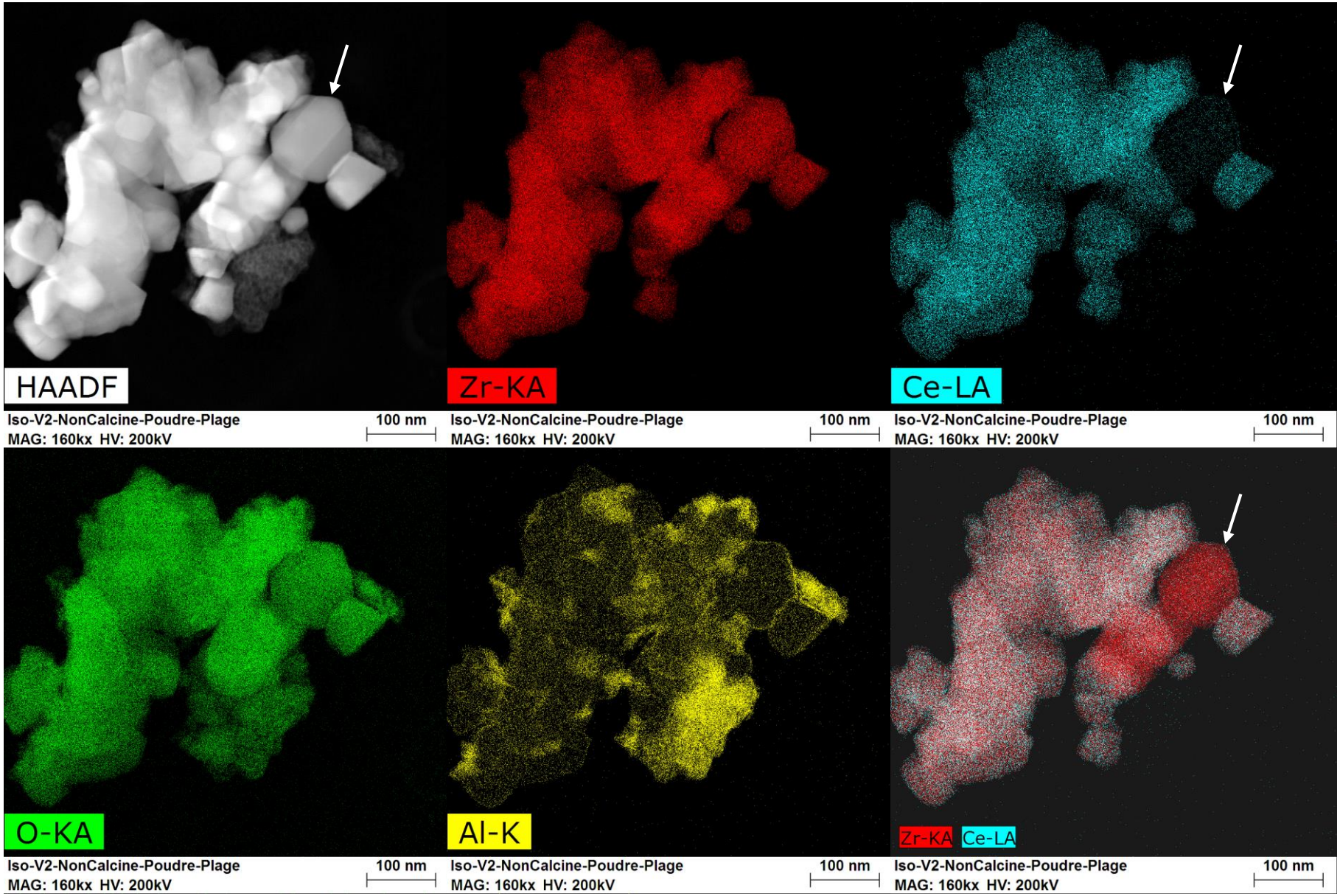
HAADF
Iso-V2-NonCalcine-Poudre-Plage
MAG: 160kx HV: 200kV
100 nm
Zr-KA
Iso-V2-NonCalcine-Poudre-Plage
MAG: 160kx HV: 200kV
100 nm
Ce-LA
Iso-V2-NonCalcine-Poudre-Plage
MAG: 160kx HV: 200kV
100 nm
O-KA
Iso-V2-NonCalcine-Poudre-Plage
MAG: 160kx HV: 200kV
100 nm
Al-K
Iso-V2-NonCalcine-Poudre-Plage
MAG: 160kx HV: 200kV
100 nm
Zr-KA Ce-LA
Iso-V2-NonCalcine-Poudre-Plage
MAG: 160kx HV: 200kV
100 nm

Fig. 2

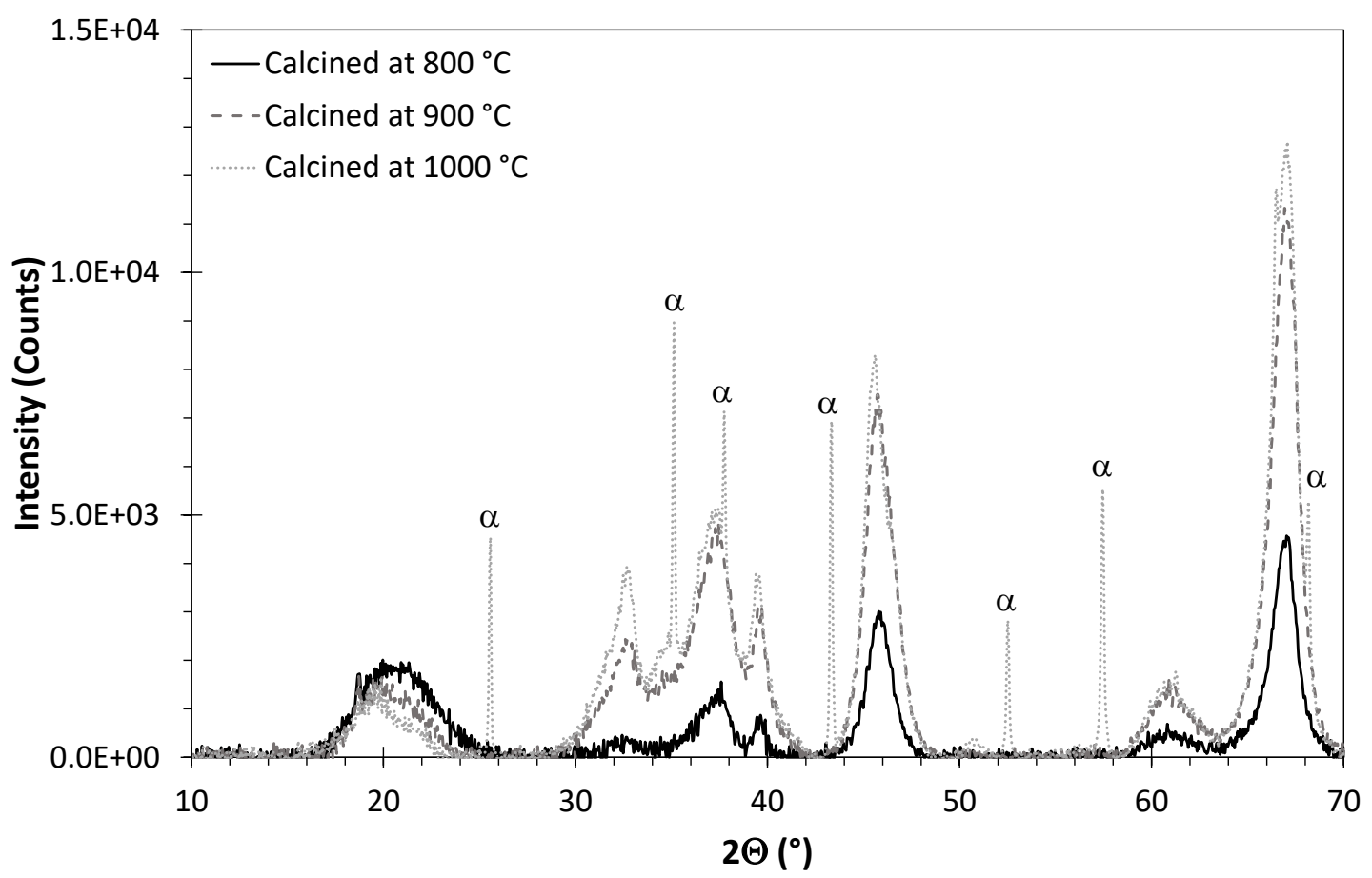
Calcined at 800 °C
Calcined at 900 °C
Calcined at 1000 °C
Intensity (Counts)
1.5E+04
1.0E+04
5.0E+03
0.0E+00
10
20
30
40
50
60
70
2Θ (°)
α

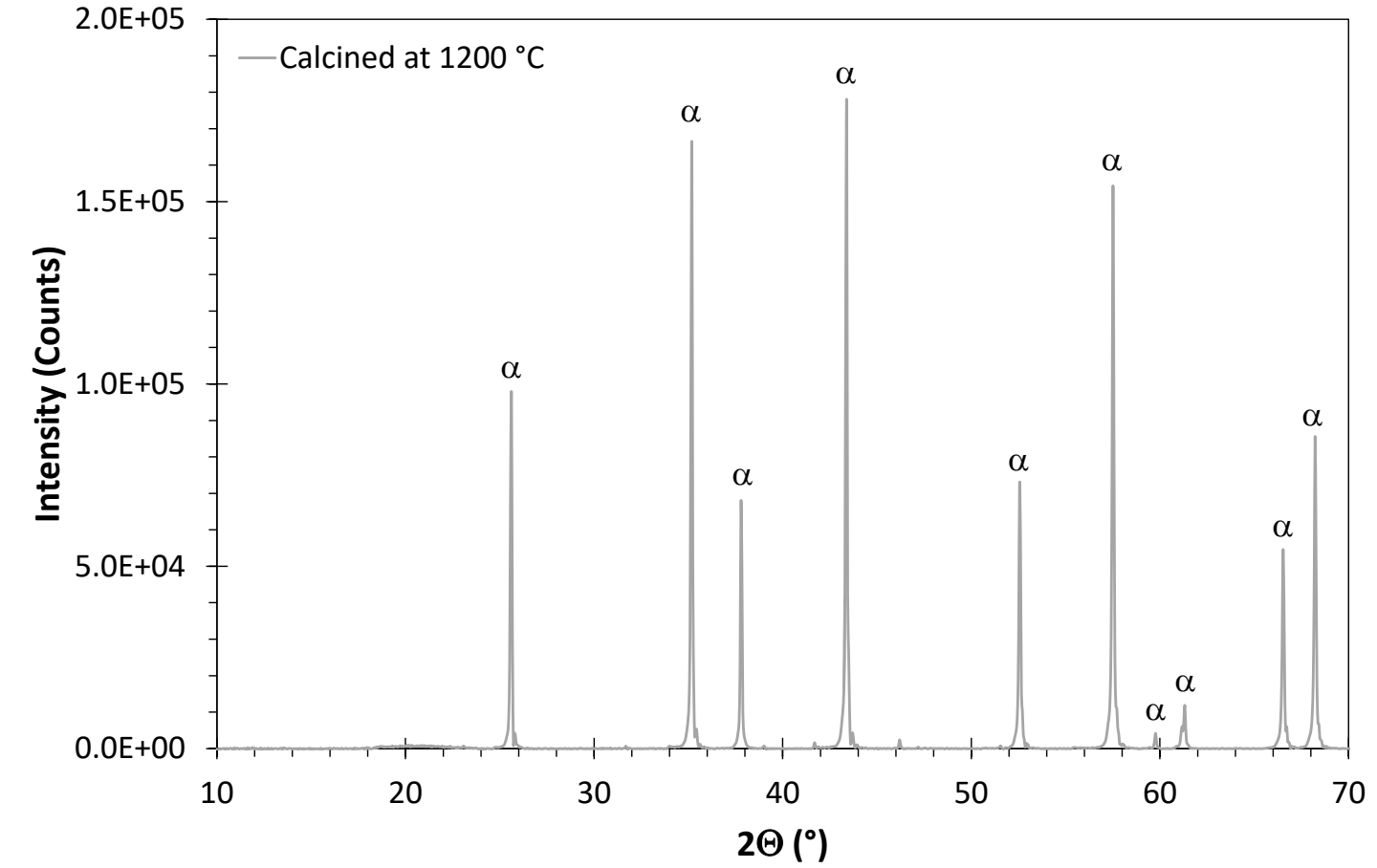
Calcined at 1200 °C
Intensity (Counts)
2.0E+05
1.5E+05
1.0E+05
5.0E+04
0.0E+00
10
20
30
40
50
60
70
2Θ (°)
α

Fig. 3

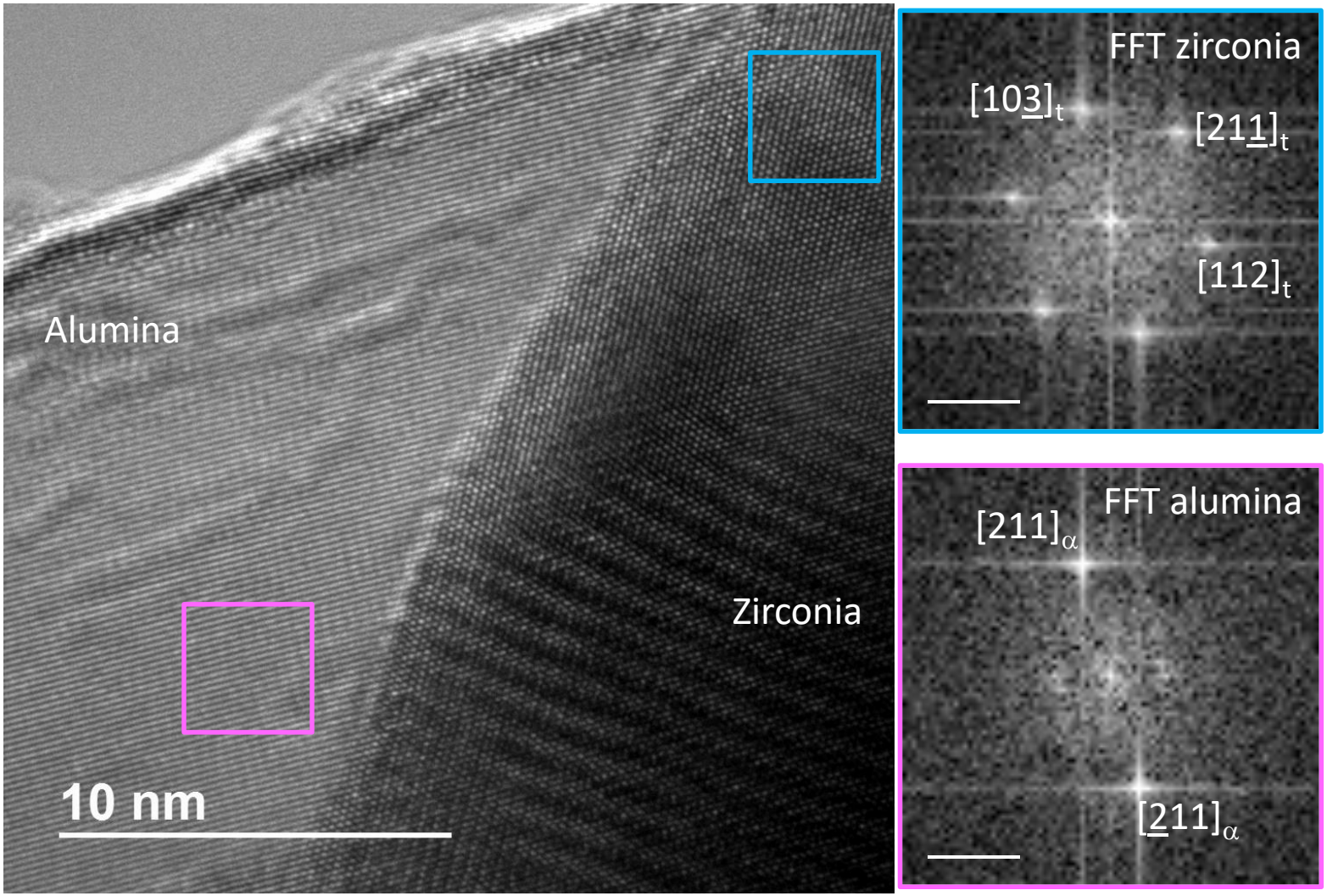
Alumina
Zirconia
10 nm
FFT zirconia
[10$\underline{3}$]$_t$
[21$\underline{1}$]$_t$
[112]$_t$
FFT alumina
[211]$_\alpha$
[$\underline{2}$11]$_\alpha$

Fig. 4

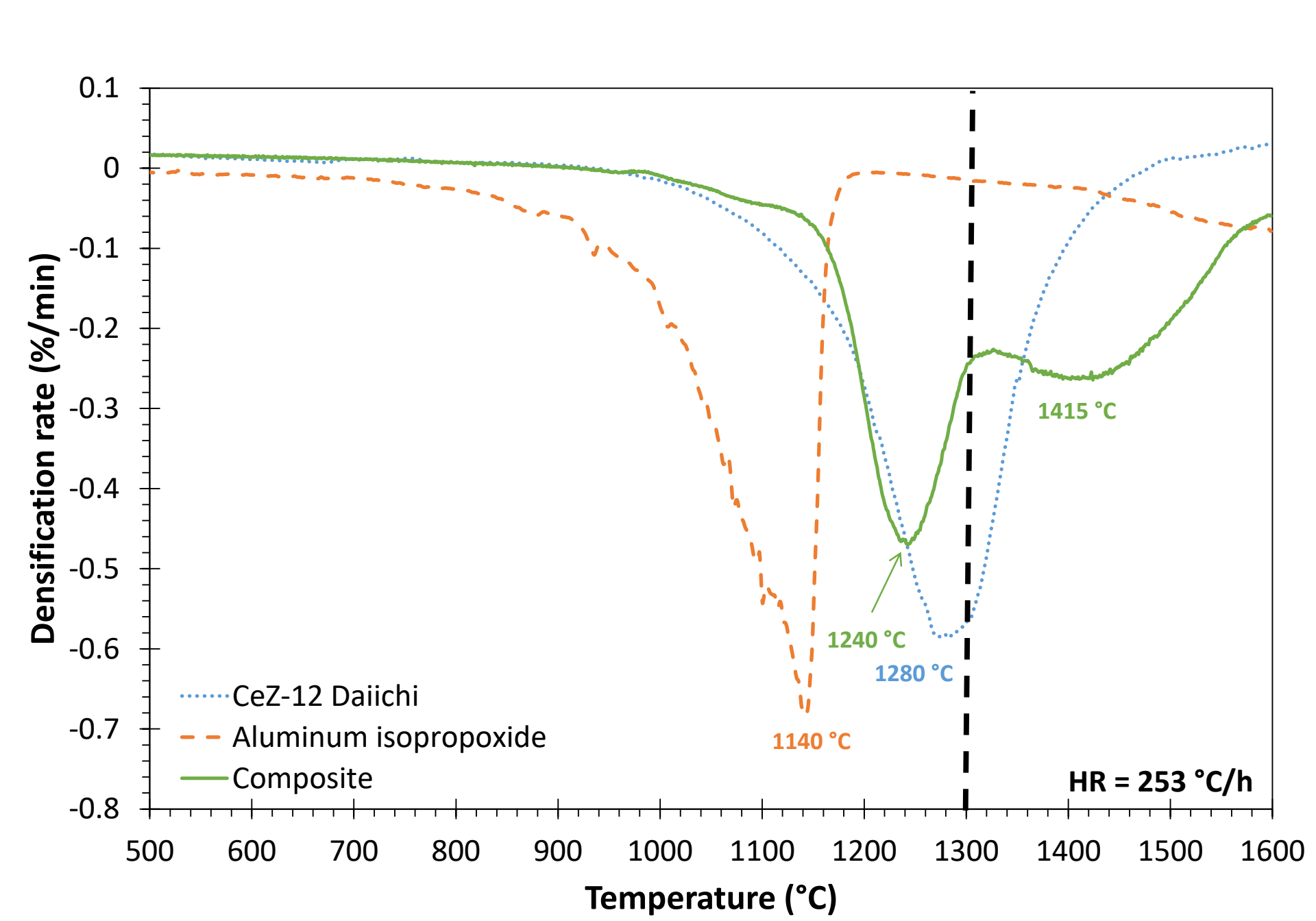
0.1
0
-0.1
-0.2
-0.3
-0.4
-0.5
-0.6
-0.7
-0.8
Densification rate (%/min)
500
600
700
800
900
1000
1100
1200
1300
1400
1500
1600
Temperature (°C)
CeZ-12 Daiichi
Aluminum isopropoxide
Composite
1140 °C
1240 °C
1280 °C
1415 °C
HR = 253 °C/h

Fig. 5

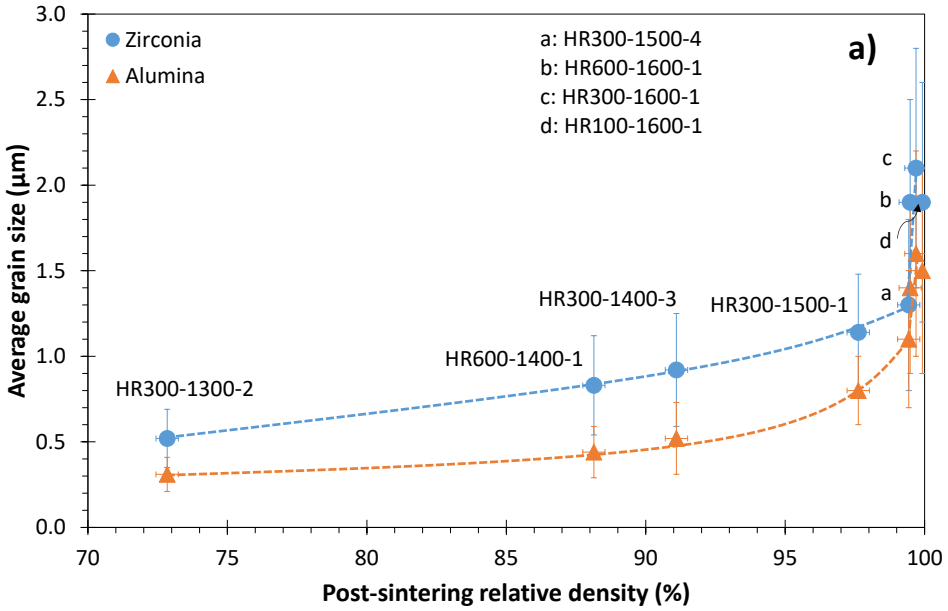
a)
Zirconia
Alumina
a: HR300-1500-4
b: HR600-1600-1
c: HR300-1600-1
d: HR100-1600-1
HR300-1300-2
HR600-1400-1
HR300-1400-3
HR300-1500-1
Average grain size (µm)
Post-sintering relative density (%)

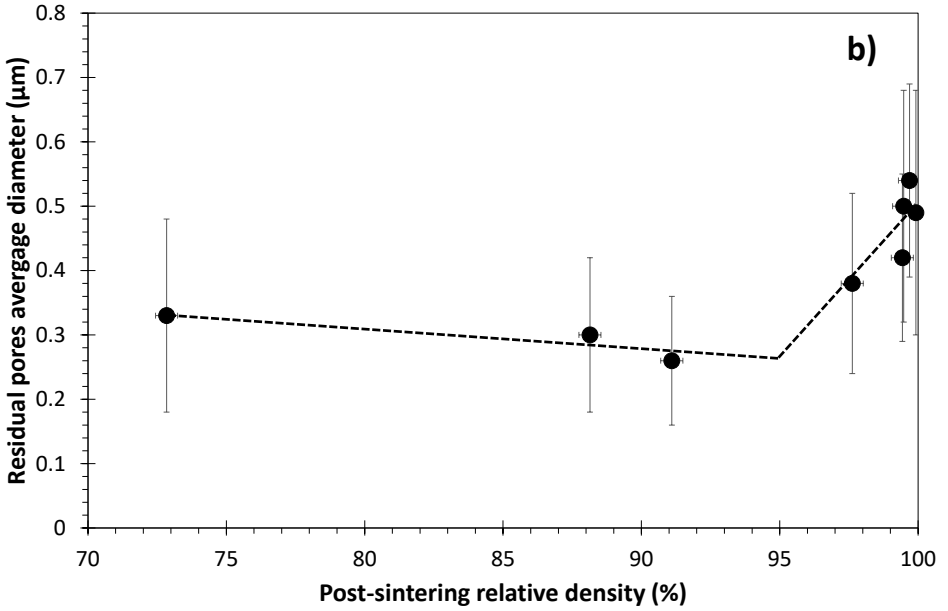
b)
Residual pores avergage diameter (µm)
Post-sintering relative density (%)

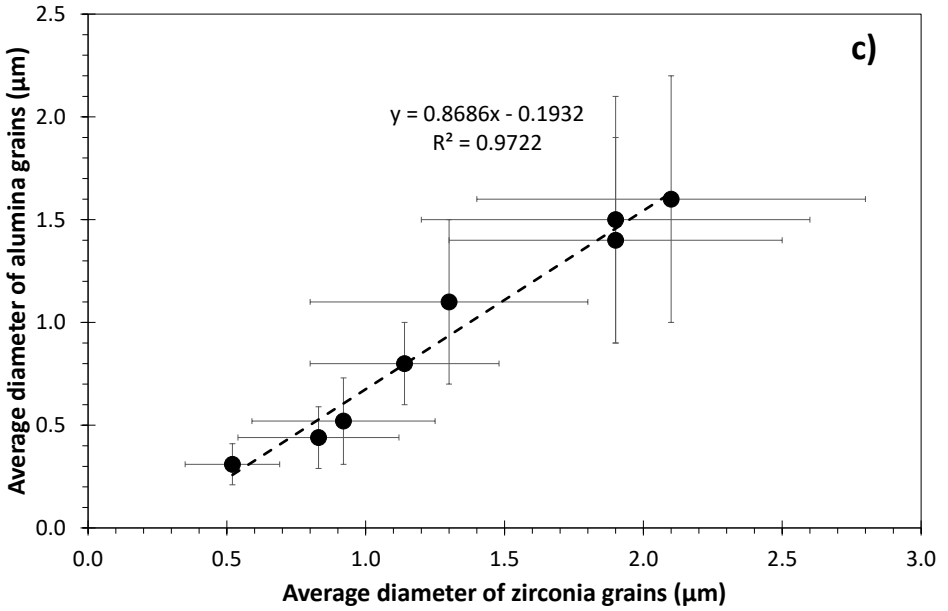
c)
y = 0.8686x - 0.1932
R² = 0.9722
Average diameter of alumina grains (µm)
Average diameter of zirconia grains (µm)

Fig. 6

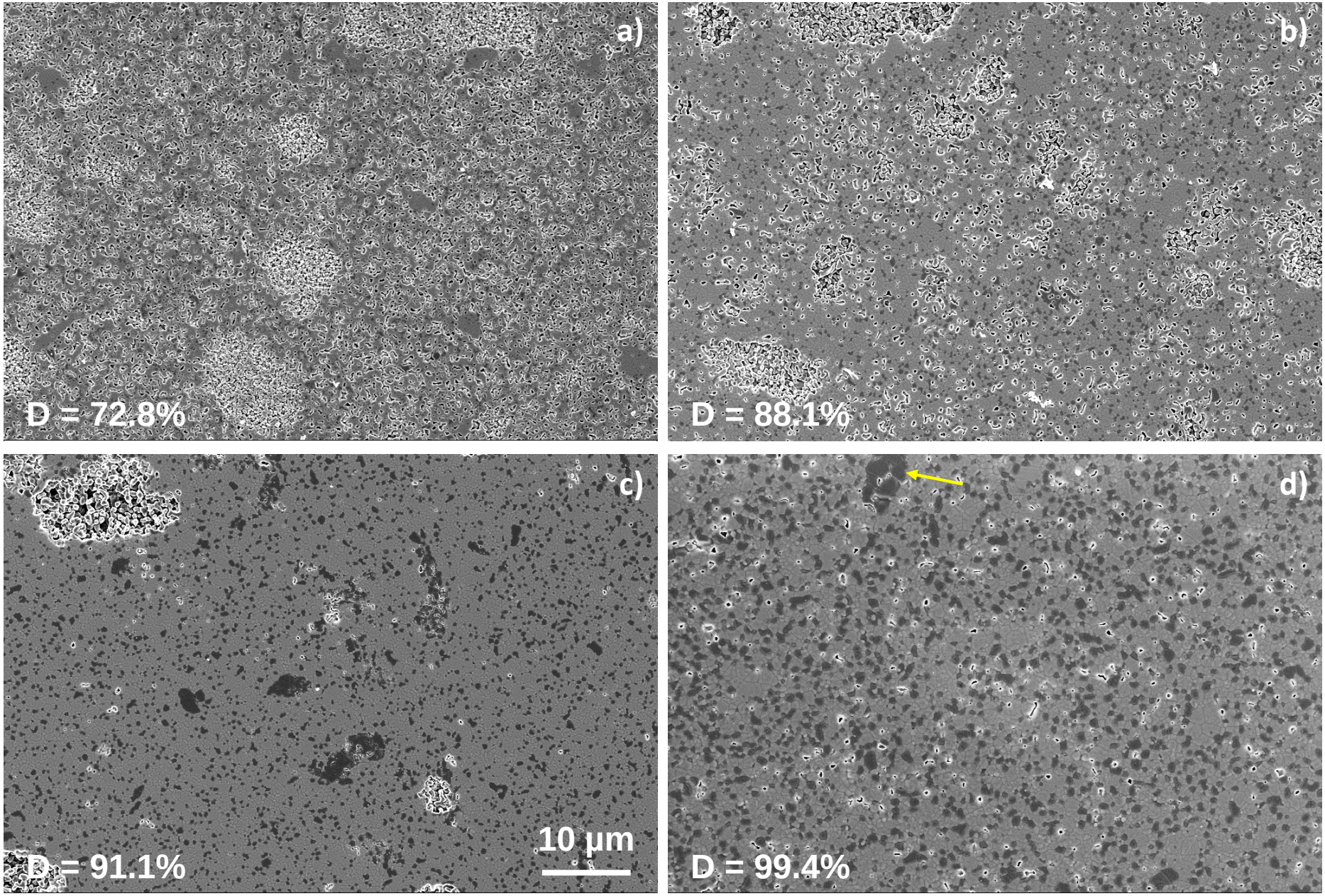

Fig. 7

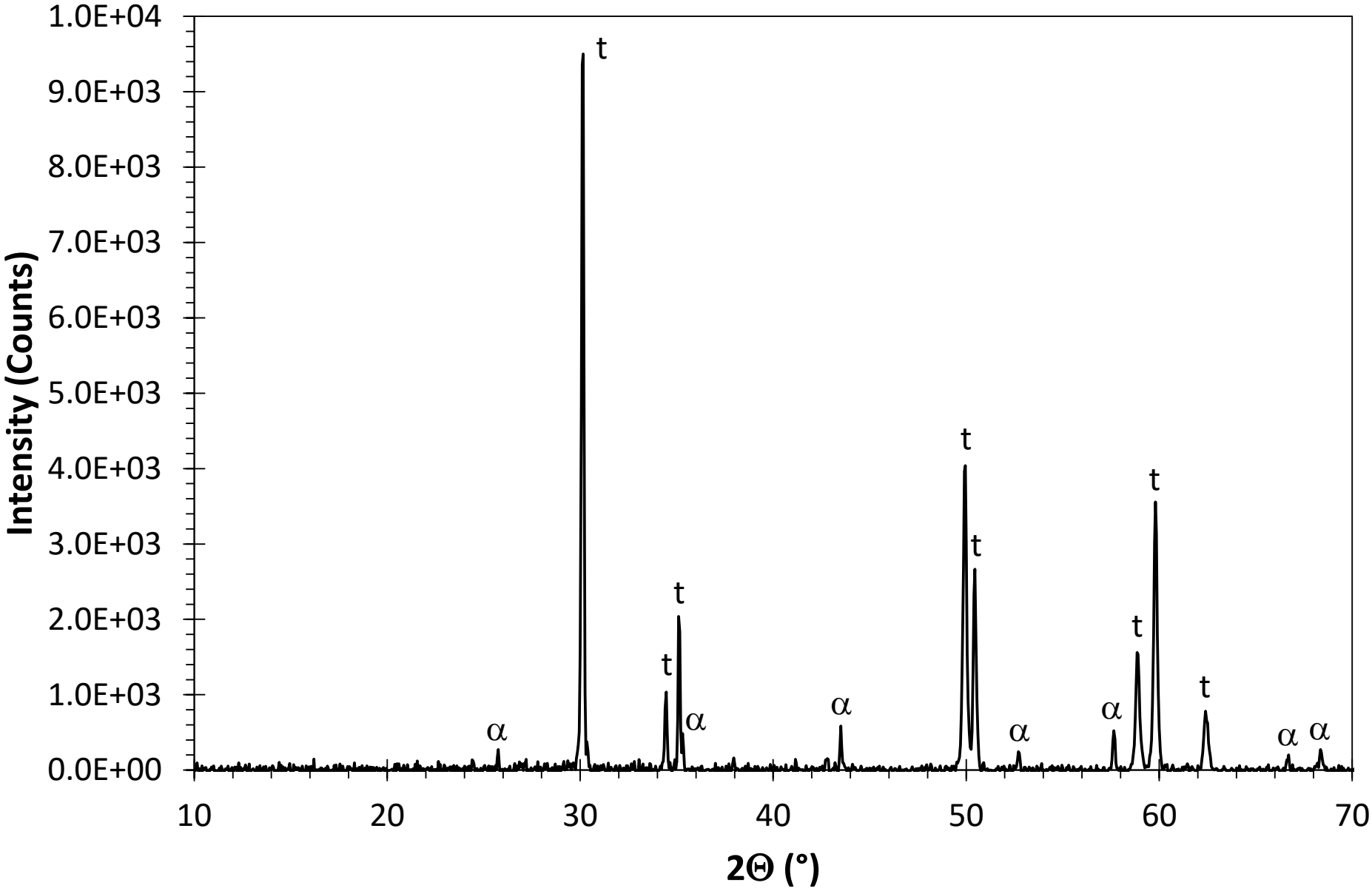
1.0E+04
9.0E+03
8.0E+03
7.0E+03
6.0E+03
5.0E+03
4.0E+03
3.0E+03
2.0E+03
1.0E+03
0.0E+00
Intensity (Counts)
10
20
30
40
50
60
70
2Θ (°)
t
α

Fig. 8

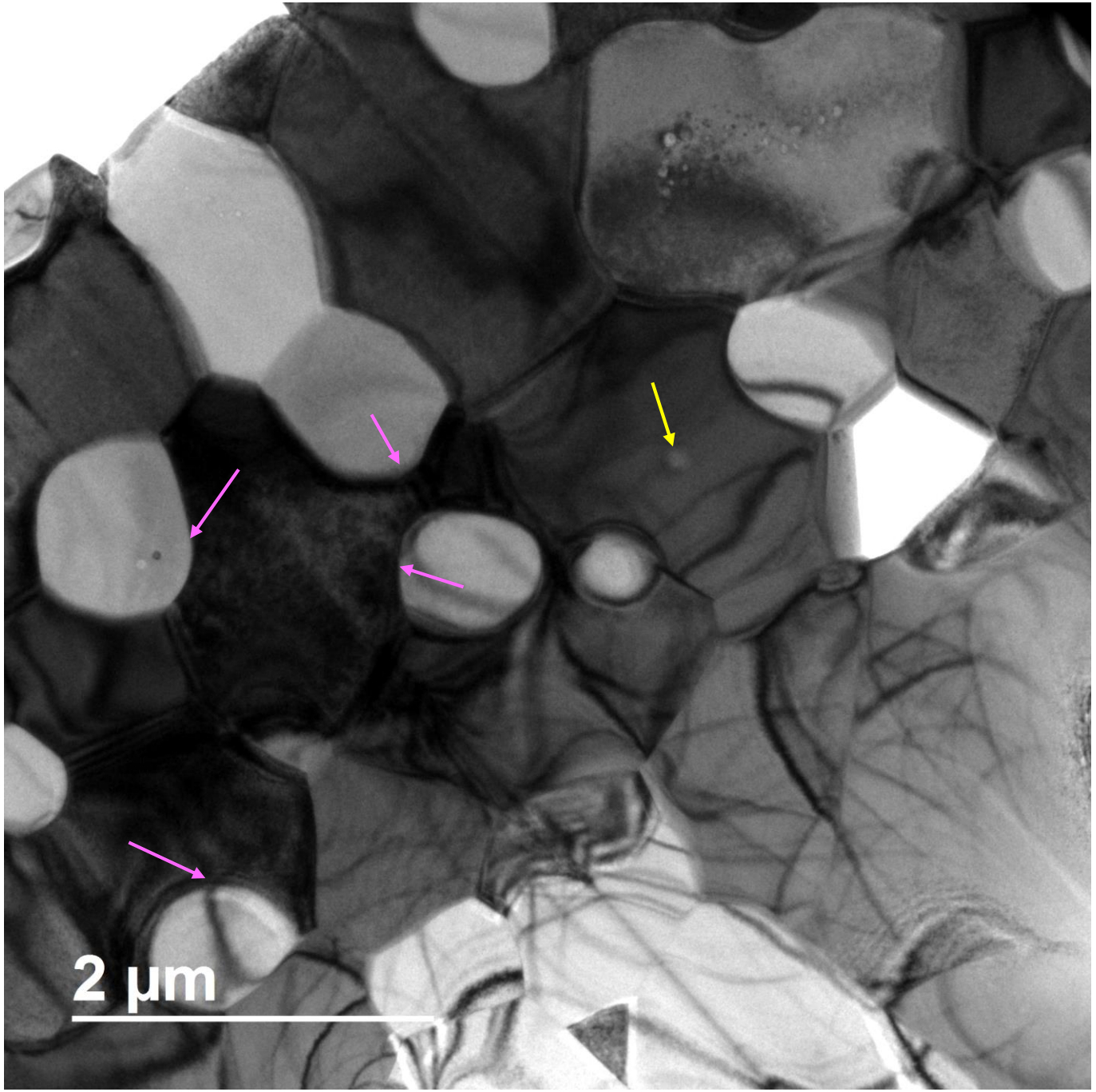

Fig. 9

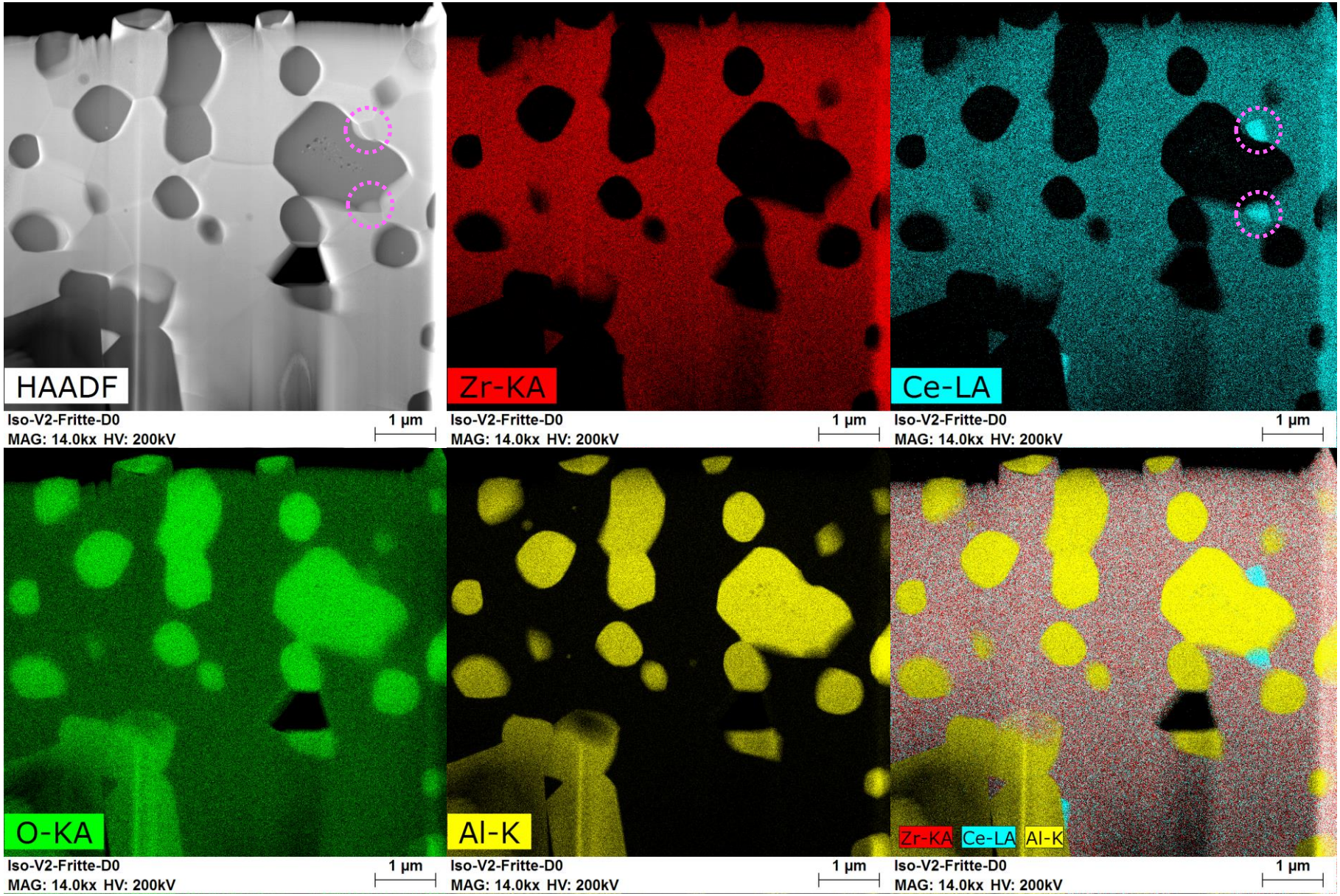
HAADF
Zr-KA
Ce-LA
O-KA
Al-K
Zr-KA Ce-LA Al-K
Iso-V2-Fritte-D0
MAG: 14.0kx HV: 200kV
1 µm

Fig. 10

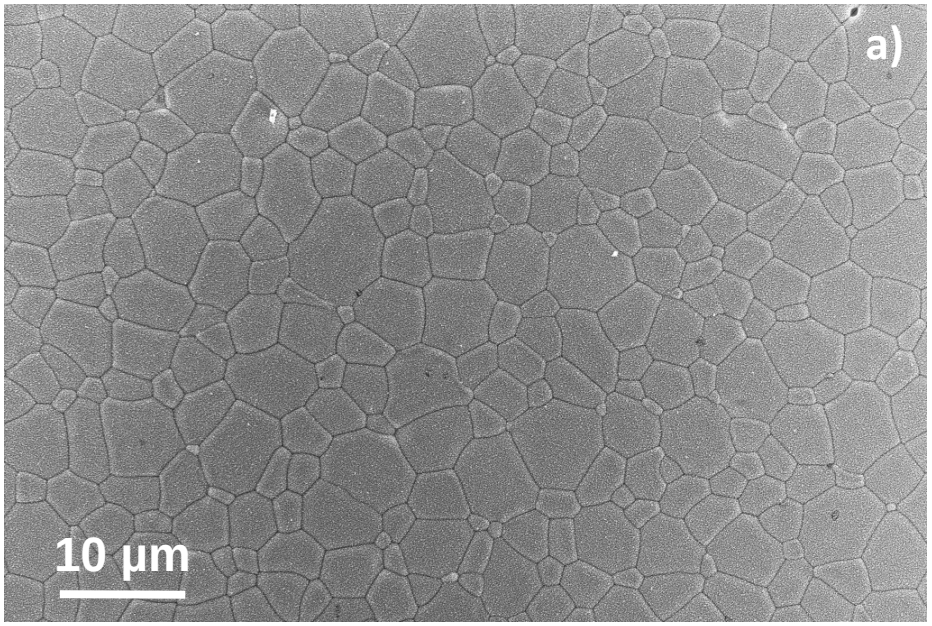
a)
10 µm

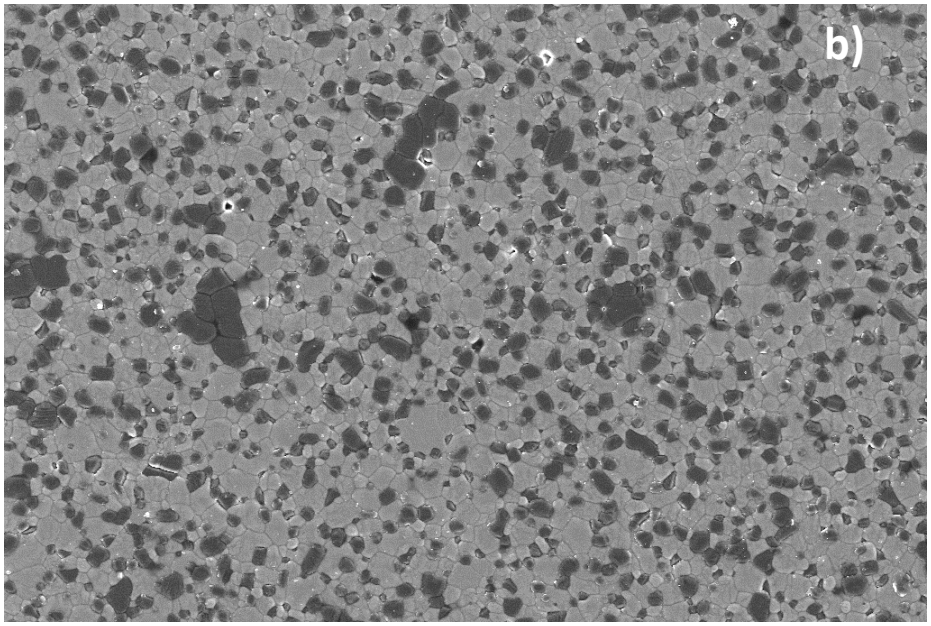
b)

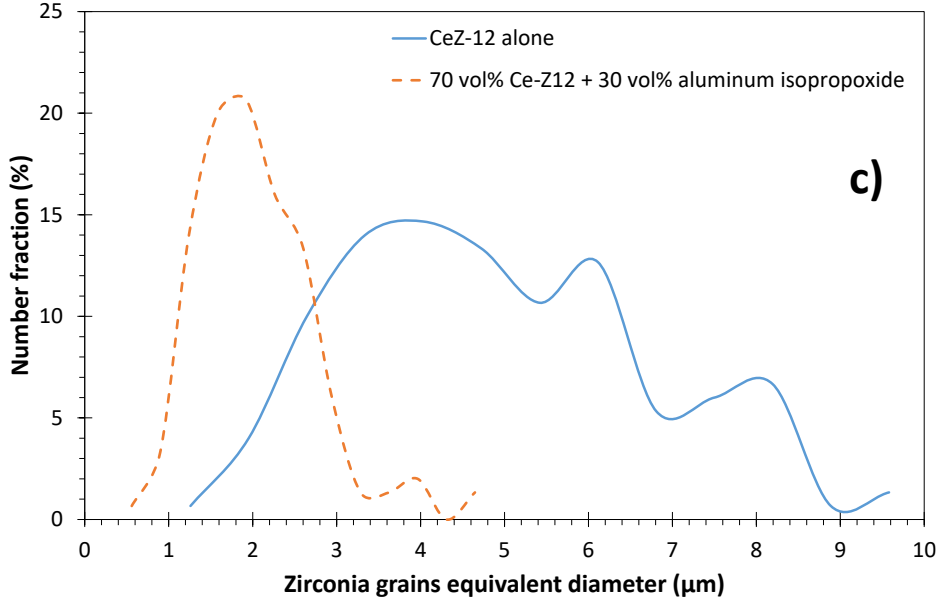
CeZ-12 alone
70 vol% Ce-Z12 + 30 vol% aluminum isopropoxide
c)
Number fraction (%)
Zirconia grains equivalent diameter (µm)
0
5
10
15
20
25
0
1
2
3
4
5
6
7
8
9
10

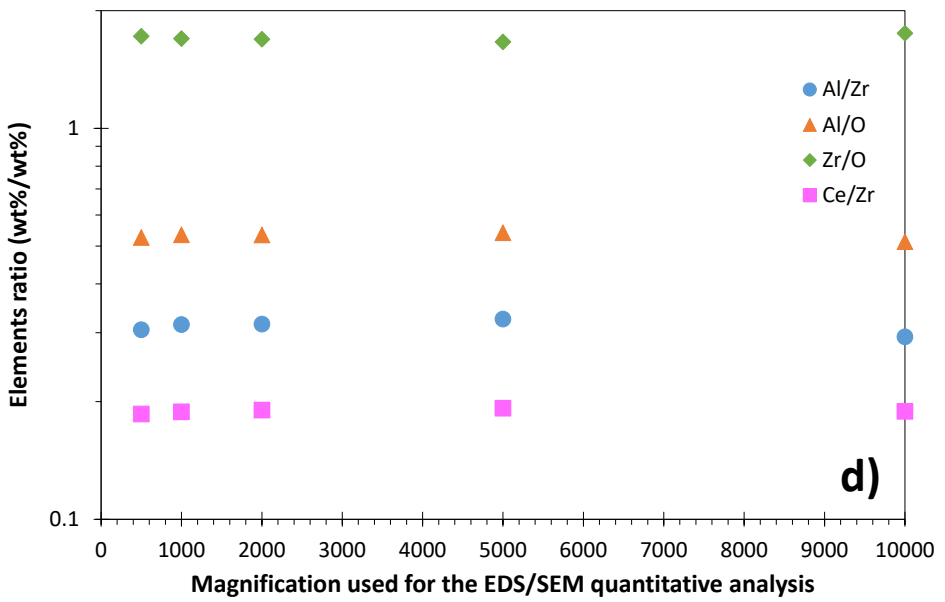
Al/Zr
Al/O
Zr/O
Ce/Zr
d)
Elements ratio (wt%/wt%)
Magnification used for the EDS/SEM quantitative analysis
0.1
1
0
1000
2000
3000
4000
5000
6000
7000
8000
9000
10000

Fig. 11

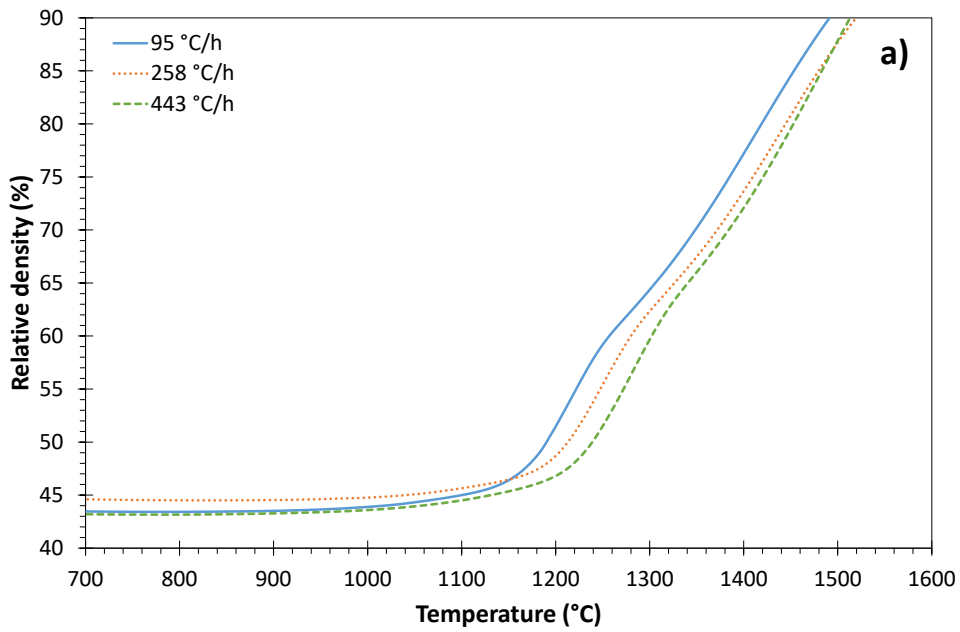
a)
95 °C/h
258 °C/h
443 °C/h
Relative density (%)
Temperature (°C)

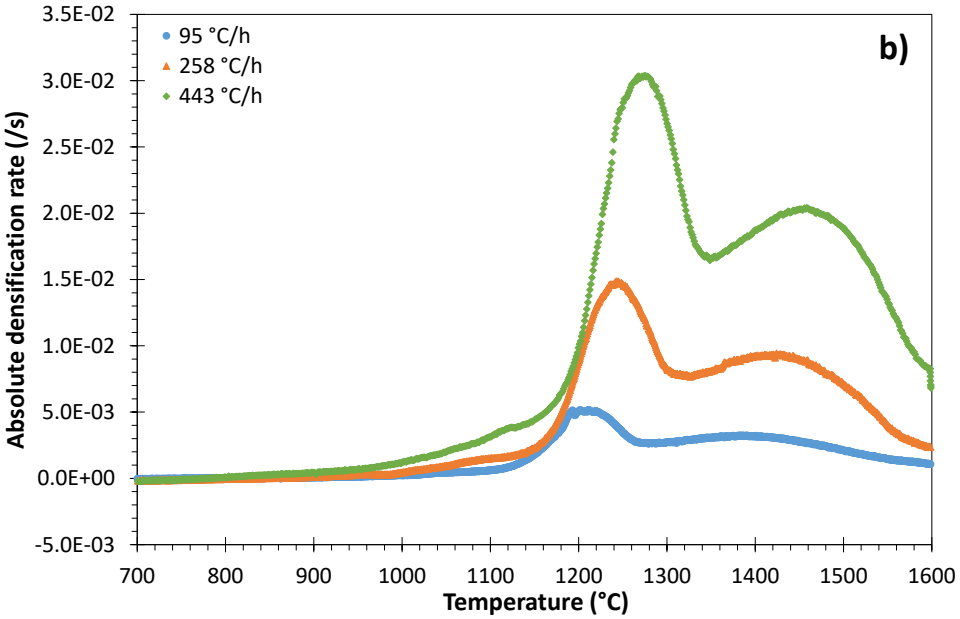
b)
95 °C/h
258 °C/h
443 °C/h
Absolute densification rate (/s)
Temperature (°C)

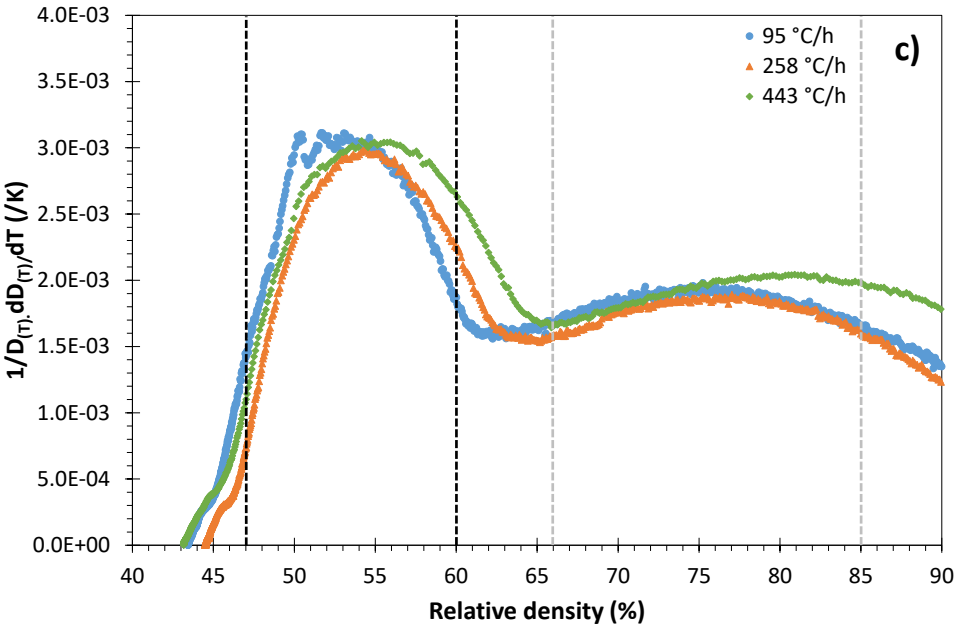
c)
95 °C/h
258 °C/h
443 °C/h
1/D(π).dD(π)/dT (/K)
Relative density (%)

Fig. 12

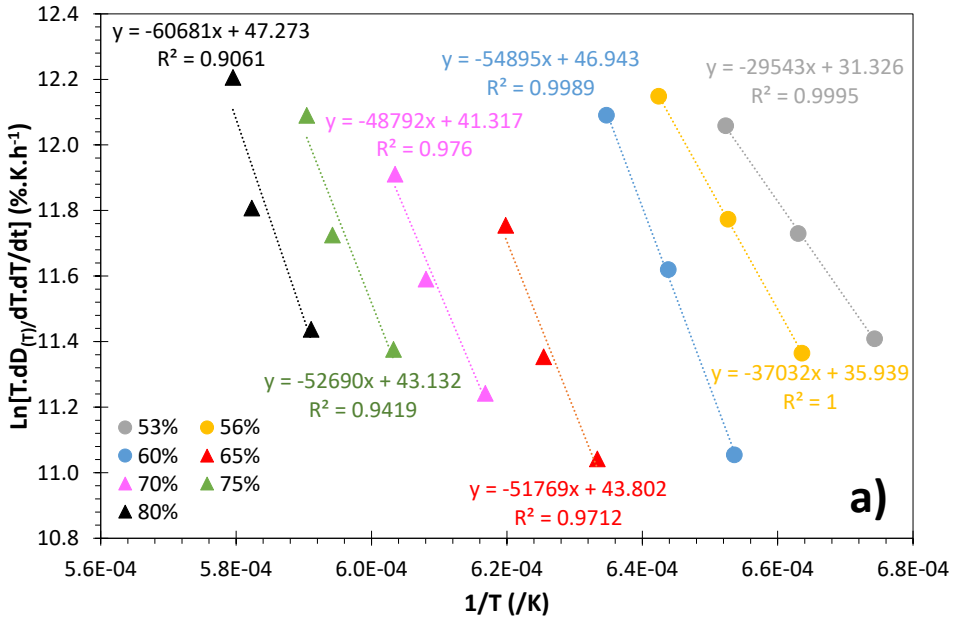
y = -60681x + 47.273
R² = 0.9061
y = -54895x + 46.943
R² = 0.9989
y = -29543x + 31.326
R² = 0.9995
y = -48792x + 41.317
R² = 0.976
y = -52690x + 43.132
R² = 0.9419
y = -37032x + 35.939
R² = 1
y = -51769x + 43.802
R² = 0.9712
53%
56%
60%
65%
70%
75%
80%
a)
Ln[T.dD(T)/dT.dT/dt] (%.K.h-1)
1/T (/K)

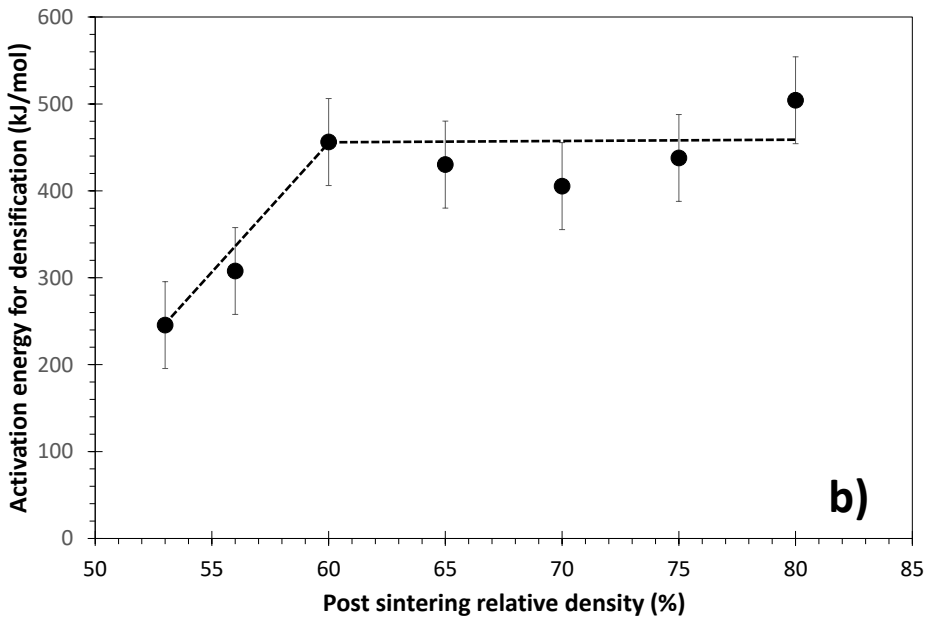
b)
Activation energy for densification (kJ/mol)
Post sintering relative density (%)

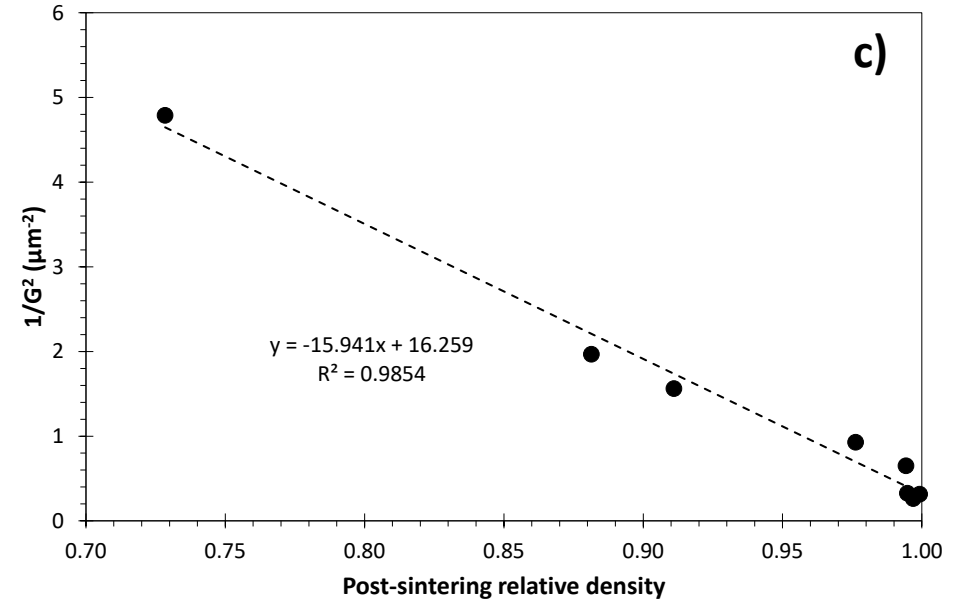
c)
y = -15.941x + 16.259
R² = 0.9854
1/G² (µm-2)
Post-sintering relative density

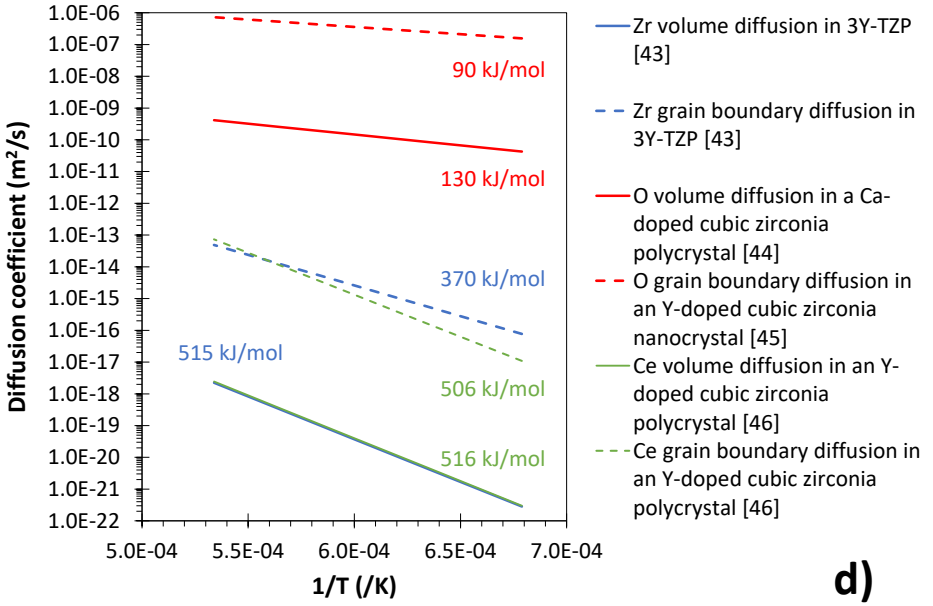
90 kJ/mol
130 kJ/mol
370 kJ/mol
515 kJ/mol
506 kJ/mol
516 kJ/mol
Zr volume diffusion in 3Y-TZP [43]
Zr grain boundary diffusion in 3Y-TZP [43]
O volume diffusion in a Ca-doped cubic zirconia polycrystal [44]
O grain boundary diffusion in an Y-doped cubic zirconia nanocrystal [45]
Ce volume diffusion in an Y-doped cubic zirconia polycrystal [46]
Ce grain boundary diffusion in an Y-doped cubic zirconia polycrystal [46]
d)
Diffusion coefficient (m²/s)
1/T (/K)

Fig. 13